Journal of Materials Research and Technology 37 (2025) 4345–4361

Contents lists available at ScienceDirect

Journal of Materials Research and Technology

journal homepage: www.elsevier.com/locate/jmrt

Towards increased strength and retained ductility of Zn–Mg-(Ag) materials for medical devices by adopting powder metallurgy processing routes

Jiří Kubásek [a,*], Selase Torkornoo [b,**], David Nečas [a], Ingrid McCarroll [b], Vojtěch Hybášek [a], Baptiste Gault [b,c], Eva Jablonská [d], Črtomir Donik [e], Irena Paulin [e], Peter Gogola [f], Martin Kusý [f], Zdeněk Míchal [d], Jaroslav Fojt [a], Miroslav Čavojský [g], Jan Duchoň [h], Markéta Jarošová [i], Jaroslav Čapek [a,h]

[a] University of Chemistry and Technology Prague, Faculty of Chemical Technology, Department of Metals and Corrosion Engineering, Technická 5, 6 – Dejvice, 166 28, Praha, Czech Republic
[b] Department of Microstructure Physics and Alloy Design, Max-Planck-Institut für Nachhaltige Materialien GmbH, Max-Planck-Straße 1, 40237, Düsseldorf, Germany
[c] Department of Materials, Imperial College London, Royal School of Mines, Exhibition Road, London, SW7 2AZ, UK
[d] University of Chemistry and Technology Prague, Department of Biochemistry and Microbiology, Technická 5, 6 – Dejvice, 166 28, Praha, Czech Republic
[e] Institute of Metals and Technology, Lepi pot 11, SI-1000, Ljubljana, Slovenia
[f] Slovak University of Technology in Bratislava, Faculty of Materials Science and Technology in Trnava, Ulica Jána Bottu 2781/25, 91724, Trnava, the Slovak Republic
[g] Institute of Materials and Machine Mechanics, Slovak Academy of Sciences, Dúbravská cesta 9/6319, 845 13, Bratislava, the Slovak Republic
[h] FZU – Institute of Physics of the Czech Academy of Sciences, Na Slovance 1999/2, 8, Prague, 18200, Czech Republic
[i] FZU – Institute of Physics of the Czech Academy of Sciences, Cukrovarnická 112/10, 6, Prague, 16200, Czech Republic

ARTICLE INFO

Keywords:
Zinc
Bioabsorbable materials
Mechanical alloying
Spark plasma sintering
Microstructure

ABSTRACT

The development of bioabsorbable zinc-based alloys with tailored mechanical properties and biocompatibility holds great promise for advancing medical implant technology. In this study, Zn–Mg and Zn–Mg–Ag alloys were synthesized using mechanical alloying (MA) followed by extrusion to achieve a combination of enhanced strength, ductility, and corrosion resistance. MA for 4 h produced ultrafine-grained powders incorporating Mg_2Zn_{11} intermetallic phases and oxide particles, which contributed to microstructure stabilization during subsequent processing. Extrusion consolidated these powders into dense materials with a uniform grain size of ~700 nm, exhibiting ultimate tensile strengths up to 435 MPa and elongation to fracture of ~12 %, representing a significant improvement over conventional processing methods. The addition of silver further enhanced the antibacterial properties, demonstrating notable efficacy against *Staphylococcus epidermidis*, while maintaining non-cytotoxic behavior *in vitro*. Corrosion rates remained low, with uniform surface degradation and the formation of protective corrosion layers. This work highlights the efficacy of combining powder metallurgy techniques to bioabsorbable zinc-based alloys with exceptional mechanical performance, corrosion behavior and *in vitro* cytocompatibility, providing a pathway for next-generation biodegradable medical devices.

1. Introduction

Zn–Mg alloys are considered perspective materials for applications in biodegradable stents or for bone fixations, especially in maxillofacial surgery, due to their reasonable corrosion rate and excellent biocompatibility [1–3]. Their function is supposed to be time-limited with complete replacement by newly healed tissue [2,4], which helps to prevent long-term issues with inflammations leading, in some cases, even to the removal of the implant as observed in other systems including Mg-based or Fe-based biodegradable materials. Localized corrosion leads to the premature loss of mechanical integrity and hydrogen gas (H_2) release casts doubts on the usability of Mg-based materials [2,4]. Fe-based materials degrade by forming iron oxides/hydroxides, which are not sufficiently soluble in the organism and may cause serious health issues [2,5]. Zinc and its alloys, on the contrary, dissolve slowly in an organism, and the corrosion reactions do not

* Corresponding author.
** Corresponding author.
E-mail addresses: kubasekj@vscht.cz (J. Kubásek), s.torkornoo@mpie.de (S. Torkornoo).

https://doi.org/10.1016/j.jmrt.2025.06.185
Received 10 April 2025; Received in revised form 23 June 2025; Accepted 24 June 2025
Available online 8 July 2025

form harmful by-products in the human body (no H-release, biocompatible corrosion products) [3,5].

Expanding the use of Zn as a bioabsorbable material requires improvements in mechanical properties, which can be achieved through alloying with suitable elements, including Ag, Cu, Li, Mg, Mn. Among them, Mg seems to be the best candidate for improving the material's strength, decreasing the modulus of elasticity [1], and positively affecting bone mineralization and overall biocompatibility [6]. The maximum solubility of Mg in the Zn matrix is near 0.3 at.% at 364 °C and decreases to almost zero at ambient temperature [2,7], leading to the precipitation of intermetallic phases [8]. These include Mg_2Zn_{11}, $MgZn_2$, Mg_7Zn_3, Mg_2Zn_3 and MgZn, which are hard and brittle, thereby improving strength but decreasing ductility. Zn–Mg materials however generally exhibit a low biodegradation rate.

Further improvement of the mechanical properties can be achieved through mechanical alloying (MA). MA causes an intensive plastic deformation during the process, which leads to the formation of alloy powders containing metastable phases. These include oversaturated solid solutions with extremely small particles and grains, reaching nanograined materials [9]. However, MA is highly dependent on the processing conditions, including the milling media and vessels, their shape and size, temperature and atmosphere during processing, and also additional control agents, such as stearic acid, which are added to prevent excessive cold welding [9,10]. Although MA technology is capable of preparing ultrafine-grained materials, the preserving of such microstructure during the consolidation at increased temperatures (>200 °C) is challenging due to the low recrystallization temperature of pure zinc (<0 °C) [11], resulting in the materials' recrystallization and coarsening, especially when the milled powder is highly stressed.

Cold isostatic pressing (CIP) and conventional sintering of green compacts [12,13], hot isostatic pressing (HIP) [13], spark plasma sintering (SPS) [13] and extrusion (E) [13,14] are generally considered for Zn-based alloys compaction. The resulting materials possess microstructures with extensive porosity, oxides and inhomogeneities in chemical and phase composition, significantly deteriorating mechanical properties. Classical sintering at an increased temperature usually takes several hours before sufficient compaction takes place, resulting in coarse-grained microstructures. A similar problem occurs during hot isostatic pressing, where materials are exposed to high temperatures for several hours, affecting the microstructure or phase composition [15–17]. The materials' recrystallization and coarsening, may be, to some extent, prevented using compaction by spark plasma sintering (SPS). SPS offers the advantage of a fast compaction technique with short times and low temperatures of the process (0.7 of the melting temperature of the metal to be compacted) [17,18]. In this technique, pulses of electric current flow through the sample and generate heat at the powder particle interfaces due to the local high resistance. Besides, the process is accompanied by adjustable compression and can produce materials with a homogeneous nonporous structure without significant grain coarsening [18–20].

Zn-alloys have also been prepared by additive manufacturing methods such as laser powder bed fusion (LPBF) [21–23]. However, based on the alloy composition, the density of the prepared materials reached a maximum of 98 %. Furthermore, the eutectic microstructure was formed along grain boundaries, and at higher magnesium concentrations (>7.7 at.%), the inhomogeneous microstructure was generated due to local precipitation of the $MgZn_2$ phase. Those issues negatively affect mechanical properties [21].

Here, we prepared materials by combining MA, SPS and extrusion, to develop a fine-grained microstructure in Zn-based alloys. As a starting material, we have selected Zn-2.6Mg (at.%) corresponding to the Zn–1Mg in wt.%, which repeatedly showed, after a conventional way of production, a good compromise between strength and ductility [3,24]. Due to the uniqueness of the materials preparation route, a main emphasis was placed on the study of the microstructure, which has subsequently serious impact on both mechanical and corrosion properties. To provide morphological, crystallographic and compositional information from millimeters to nanometers, we combined scanning-electron microscopy (SEM), transmission electron microscopy (TEM) and atom probe tomography (APT). In particular, APT provides detailed information about the material's nanoscale composition in 3D, though serving as a very helpful complementary technique for conventional 2D imaging techniques such as electron microscopy. Furthermore, we investigated how the addition of Ag affects the microstructure, mechanical performance and dissolution of the material. Here, we discuss the details of the microstructure-property relationships in these alloys and demonstrate their high potential for direct application as bioabsorbable metals.

2. Materials and methods

2.1. Materials synthesis

The Zn-2.6Mg and Zn-2.6Mg-0.6Ag alloys were prepared by mechanical alloying (MA) for 4 h using 800 rotation per minute (RPM) in a Retch E-max mill equipped with a water-cooling system capable of maintaining a temperature below 50 °C. The powders used were pure Zn (99.9 %, particle size <149 μm, Alfa Aesar), Mg (99.8 %, particle size <44 μm, Alfa Aesar) and silver (99.9 %, particle size <20 μm, Safina a. s.). The ball-to-powder ratio (B/P ratio) was selected as 5:1. The grinding process was carried out using zirconia balls in a 125 ml elliptically designed vessel with zirconia coating. To prevent powder agglomeration during the mechanical alloying, 0.03g stearic acid was added to the powder mixture before milling. Materials were mechanically alloyed under a protective Ar atmosphere (99.96 %). The MA parameters were selected based on several experiments documenting the effect of various parameters on powder properties. Two methods of compaction of alloyed powders were selected. Firstly, the fast compaction method – spark plasma sintering (SPS - FCT Systeme HP-D 10) was performed at 300 °C, 80 MPa pressure for 10 min in graphite tools under a protective Ar atmosphere (99.96 %). Secondly, the Zn–2.6Mg alloy was compacted by hot extrusion at 200 °C with an extrusion ratio (ER) equal to 25. Before extrusion, "green compact" from powders were produced in the form of cylinders with 30 mm in diameter and 50 mm high by vacuum hot pressing (HVP) at 200 °C for 2 h. The designation of the synthesized materials is shown in Table 1. The chemical composition of the prepared powders and compacted materials was verified by atomic absorption spectrometry - AAS (Agilent 280 FS AA spectrometer).

2.2. Microstructure

The prepared samples were first ground on SiC papers P400 – P2500, then polished on diamond paste D2 (UR-Diamant), and finally polished on the Eposile NonDry suspension (QATM) for 20 min. The microstructure was characterized using an SEM (TESCAN VEGA 3 LMU) with an EDS analyzer (OXFORD Instruments AZtec). Additionally, electron

Table 1
The materials designation and processing conditions.

Materials designation	Alloy composition [at. %]	Alloy composition [wt. %]	Mechanical alloying	Compaction method and conditions
Zn-2.6Mg$^{(4h)}$	Zn-2.6Mg	Zn–1Mg	800RPM, 4h, BP = 5:1	–
Zn-2.6Mg-0.6Ag$^{(4h)}$	Zn-2.6Mg-0.6Ag	Zn–1Mg–1Ag	800RPM, 4h, BP = 5:1	–
Zn-2.6Mg$^{(4h)}$ + Ex	Zn-2.6Mg	Zn–1Mg	800RPM, 4 h, BP = 5:1	Extrusion, 200 °C, ER25
Zn-2.6Mg-0.6Ag$^{(4h)}$ + Ex	Zn-2.6Mg-0.6Ag	Zn–1Mg–1Ag	800RPM, 4 h	Extrusion, 200 °C, ER25

backscattered diffraction (EBSD) analyses were performed on an Apreo 2 SEM using an acceleration voltage of 15 kV with a probe current of 13 nA after final polishing was performed using OPS for 20 min. EBSD Kikuchi patterns were measured with a Symmetry S3 camera (Oxford instruments) using AZtec software. Samples were tilted 70° for measurements and an acceleration voltage of 15 kV of used. The data were processed using AZtecCrystal software. Observation and documentation of the microstructure at a nanoscale was performed using a FEI Tecnai TF20 X-twin field emission gun transmission electron microscope (TEM) operated at 200 kV and equipped with an EDS detector. Particularly, scanning transmission electron microscopy (STEM) mode was used for the microstructure observation. For STEM, Z-contrast imaging was performed using a high-angle annular dark field (STEM–HAADF) detector. Samples for TEM analyses were prepared using a JEOL ION SLICER EM 09100 IS with a voltage of 5 kV and a current of 120 μA. The phase composition was measured by X-ray diffraction (X'Pert^3 Powder instrument in Bragg-Brentan geometry using a Cu anode ($\lambda = 1.5418$, U = 40 kV, I = 30 mA). Quantitative phase analysis was carried out using the whole pattern Rietveld refinement software MAUD [25]. The theoretical porosity was calculated from the prepared samples' weight, volume, and density. Image analyses in ImageJ software measured the grain size.

A 2.5 μm × 20 μm region of the polished sample was coated with 1 μm of platinum carbon (Pt–C) using a gas-injection system inside a dual-beam scanning electron microscope/focused ion beam (SEM/Ga FIB) (FEI Helios Nano-Lab 600i) (FEI Company, Hillsboro, OR, USA) at 3.0 kV and 1.4 nA. A trench was milled using a voltage of 30 kV and a current of 2.5 nA on each side of the Pt–C-coated lamella. Next, 3 μm × 3 μm of the lamella edge was milled at 30 kV and 0.23 nA to attach the 2.5 μm × 20 μm lamella to the OmniProbe 200 Nanomanipulator (Oxford Instruments, Abingdon, UK) with Pt–C. Lamella (2.5 μm × 2 μm) were mounted onto Presharpened Microtip™ Coupons (PSM M36) (CAMECA Instruments, Madison, WI, USA) and sharpened into needle-like shapes with a diameter of 30–100 nm. The Zn–1Mg$^{(4h)\ +\ Ex}$ sample was analyzed in the LEAP™ 5000 XR (CAMECA Instruments, Madison, WI, USA using a laser pulse energy of 50 pJ, a base temperature of 50 K, and a repetition rate of 125 kHz, and the detection rate was fixed at 5 ions detected per 1000 pulses on average. The Zn–1Mg$^{(8h)\ +\ Ex}$ sample was analyzed in the LEAP™ 5000 XR (CAMECA Instruments, Madison, WI, USA using a pulse fraction of 20 %, a base temperature of 50 K, and a repetition rate of 200 kHz, and the detection rate was fixed at 5 ions detected per 1000 pulses on average. The Zn–1Mg–1Ag$^{(4h)\ +\ Ex}$ sample was analyzed in the LEAP™ 5000 XS (CAMECA Instruments, Madison, WI, USA using a pulse fraction of 20 %, a base temperature of 50 K, and a repetition rate of 500 kHz, and the detection rate was fixed at 5 ions detected per 1000 pulses on average. The reconstruction of all datasets and analysis were performed in CAMECA Instruments APSUITE (version 6.3.0.90).

2.3. Mechanical properties

The mechanical properties of the prepared alloys were characterized by Vickers hardness and tensile tests. HV1 was measured on a Future-Tech FM-100 at a load of 1 kg for 10 s. Tensile tests were performed using an Instron 8802 instrument on "dog bone" specimens (Fig. S1 – supplementary file), respectively, at a strain rate of 0.003 s^{-1}.

2.4. Corrosion behaviour

To describe the corrosion properties of the material, a 7-day exposure was performed, extended by non-destructive electrochemical measurements: open circuit potential (OCP), electrochemical impedance spectroscopy (EIS) and polarization resistance (R_P). Measurement was performed in a complex body simulation, i.e. in EMEM M7278 with 5 % FBS (Foetal Bovine Serum, Sigma Aldrich) and the necessary addition of 1 % antibiotics/antimycotics (all Sigma Aldrich) at 37 °C. Cylindrical samples 10 mm high and 4.3 mm in diameter were ground (to FEPA P2500), washed with demi-water and degreased in ethanol. Samples were further, mounted on a PTFE (Polytetrafluoroethylene) holder immediately before measurement. Subsequently, the samples, together with glassy carbon rods and a 75 ml polymethylpentene cell, were sterilized using UV-C (ultraviolet light in the wavelength range of 100–280 nm (nm). Afterwards, the measuring cell was assembled and an ethanol-washed silver-chloride reference electrode (SSCE - Silver/Silver Chloride Electrode, 3 mol/KCl) was added. During the subsequent exposure, OCP was acquired, intermittently by R_P measurement (+-15 mV/OCP, 0.125 mV/s) or EIS (60 kHz − 0.01 Hz, 7 points per decade, E_{AC} 15 mV.rms, E_{DC}=OCP). Measurements were performed on a Gamry Reference 600 potentiostat, the correctness of the impedance data was verified by Kramers-Kronig transformation in Gamry Echem Analyst software, and subsequent evaluation was performed in ZView software. The material was also analyzed after exposure using SEM/EDS Tescan Vega 3 and OXFORD Instruments AZtec and a light microscope Olympus SZX10 (LM).

2.5. In vitro biological behavior

2.5.1. In vitro cytotoxicity test - test on extracts

Human foetal osteoblasts hFOB 1.19 (ATCC® CRL-11372™) were maintained in DMEM/Ham's F-12 (Sigma, D6434) medium with 10 % FBS (Foetal bovine serum - Sigma F7524), 2.5 mM L-glutamine in the form of stable dipeptide (Sigma, 8541) and selection reagent G418 (Sigma, G8168) at a permissive temperature of 34 °C, with 5 % CO_2 and 100 % relative humidity. Cells were passaged regularly using a trypsin-EDTA solution without phenol red (Gibco, 15400054). Cells were used from the 3rd passage after thawing and only until the 15th passage.

On day 1, hFOB 1.19 cells were trypsinized and resuspended in the cultivation medium to obtain a suspension with a concentration of $2{\cdot}10^5$ cells per mL. Subsequently, 100 μl of the cell suspension was seeded in a 96-well plate, which means the seeding density of $2{\cdot}10^4$ cells per well.

Cylindrical samples (height 10 mm, diameter 4 mm) of the alloys (Zn-2.6Mg$^{(4h)\ +\ Ex}$ and Zn-2.6Mg-0.6Ag$^{(4h)\ +\ Ex}$) were weighed, sterilized by 70 % ethanol (2 h) and by UV light (2 h). Thereafter, samples were transferred to a cultivation medium L-15 (Leibovitz's L-15 medium) supplemented with reduced concentration of FBS (5 %, as suggested by ISO 10993-5 standard) without G418 and agitated (130 RPM) at 37 °C in closed vessels for 24 h. The surface-to-volume ratio stated in the ISO 10993-12 (1.25 cm^2 mL^{-1}) was adjusted as recommended for degradable metals [26] i.e. the volume was five times higher. Three replicates were used for the alloys tested.

On day two, the medium in 96-well plates was replaced by the extracts prepared as described above. The extracts were used undiluted (100 % extracts) and twice diluted (50 % extracts). Six technical replicates were used for each sample. Sole cultivation medium L-15 served as negative (unaffected) control. The concentration of released ions in the extracts was measured by AAS.

On day three, after 24 ± 1 h of incubation with the extracts at 37 °C without CO_2, the cell metabolic activity was evaluated by a resazurin assay. Resazurin is metabolized to resorufin by living cells. The extracts were removed and a resazurin solution (final concentration 25 μg mL^{-1}) in Hank's balanced salt solution (HBSS) was added. After 2 h, fluorescence at 560/590 nm (excitation/emission) was measured (Fluoroskan Ascent FL, Thermo). Cytotoxicity of the extracts was calculated as a percentage of the metabolic activity of the negative control. Extracts causing a decrease below 70 % of the activity of the negative control were considered cytotoxic, as described in the ISO 10993-5 standard.

2.5.2. Antibacterial tests

Antibacterial tests were performed with *Escherichia coli* (DBM 3138) as a representative of Gram-negative bacteria and *Staphylococcus epidermidis* (ATCC14998 CCM21245) representing Gram-positive bacteria. The test conditions were adopted from Ref. [27].

A bacterial suspension was prepared the day before the test. The bacteria were inoculated into the liquid Luria-Bertani (LB) medium (Lennox) and incubated at 37 °C overnight. On the day of the experiment, the bacterial suspension was diluted with phosphate-buffered saline (PBS) to a turbidity of 1 McFarland standard (which corresponds to approx. $3{\cdot}10^8$ colony forming units, CFU/mL for *E. coli*). Subsequently, a serial dilution was prepared; the sixth decimal and fourth decimal dilutions were used for *E. coli* and *S. epidermidis*, respectively. The specimens Zn-2.6Mg$^{(4h)+Ex}$ and Zn-2.6Mg-0.6Ag$^{(4h)+Ex}$ (height 3 mm, diameter 4 mm) were sterilized in 70 % ethanol (2 h) and under UV light (2 h) and then submerged in 0.5 ml of bacterial suspension (the surface to volume ratio was 1.25 cm^2 per mL). The samples were incubated in bacterial suspensions for 4 h at laboratory temperature. Three replicates were used for each type of material. Copper was used as a positive (antibacterial) control. The negative control (suspension without samples) was used as a control of bacterial growth.

After 4 h, the drip test was performed by transferring 25 μL of suspension into each field of Petri dish (LB agar for *E. coli* and plate count agar, PCA for *S. epidermidis*) divided into twelve squares. A Petri dish contained four drops (of 25 μL) of each triplicate of one specimen. Thus, every type of sample was applied on one plate. Blank (pure PBS) and a control dish (bacterial suspension without samples) were prepared using the same drip method. Furthermore, a subsequent 1:1 dilution of each suspension was performed with PBS to ensure the countability of the colonies in the case of too large number of colonies in the original suspensions. The plates were then left at laboratory temperature and, if necessary, the next day transferred to 37 °C until the colonies on the control plate were visible and suitable for counting. Colonies on plates were counted using the Schuett Count device. The colonies counts were compared to the count in the control dish. Furthermore, the same set of samples was sterilized and incubated for 4 h in the same volume of PBS as for the antibacterial test. The concentration of released Zn was measured by AAS.

3. Results

3.1. Microstructure

3.1.1. Processing of powders by mechanical alloying

Electron micrographs of the supplied powders are displayed in Fig. S2 (supplementary file). These powders were combined in appropriate volumes in the milling vessels to produce mechanically alloyed powders.

Firstly, we have studied the effect of long-term high-energy MA on the microstructure development of the Zn-2.6Mg alloy, including phase and chemical composition. Both MA powders were very fine, without agglomerates, due to controlled milling parameters and the addition of stearic acid (Fig. 1). The powder particles were further characterized by sharp edges and a layered structure, which is caused by the repeated cold welding of the input particles and their subsequent breakage. The individual particles were up to 90 μm in size; however, the main fraction was 30 ± 17 μm for Zn-2.6Mg$^{(4h)}$ and 24 ± 12 μm for Zn-2.6Mg-0.6Ag$^{(4h)}$. The final size of the alloy powders is reduced compared to the input zinc powder. We expect that this is affected by two main factors. Firstly, prolonged exposure to temperature-controlled MA crushes the powder by the impact of the grinding balls. Secondly, due to the low magnesium solubility in zinc, it is likely that brittle intermetallic phases precipitate during the milling and support the disintegration of larger particles. Such behavior is supported by the identification of the Mg_2Zn_{11} phase in the milled powder by X-ray diffraction (Table 2 and Fig. 4).

Furthermore, the XRD results of MA powders (Table 2, Fig. 2) revealed no $MgZn_2$ although metastable conditions could lead to its formation. Our previous work has shown that mechanical alloying at 800 RPM leads to the formation of alloy in a shorter time (4 h) than at lower RPM values [28]. Increasing the milling time to 8 h led even to the dissolution of almost all the input magnesium in the Zn matrix. Subsequent AAS analyses of the MA powders confirmed that the composition is as designed, proving there were no selective losses of Mg in the milling vessels during the process.

3.1.2. Consolidated materials

Fig. 3 shows the phase composition of compacted Zn–Mg-(Ag) materials with the evaluated results reported in Table 2. The compacted Zn-2.6Mg$^{(4h)+Ex}$ and Zn-2.6Mg-0.6Ag$^{(4h)+Ex}$ materials exhibited comparable phase composition as the powder precursors. The slight increase in the content of Mg_2Zn_{11} in the extruded products can be attributed to the further precipitation of Mg_2Zn_{11} during the consolidation process. Besides, traces of MgO were observed by detailed analyses in similar amounts in powder precursors and compacted materials indicating some preferential oxidation of Mg. It is worth mentioning that MgO diffraction

Table 2
The phase composition of prepared MA powders and compacted products according to XRD.

Material	conditions	Phase composition [wt.%]			
		Zn	Mg_2Zn_{11}	$Ag_{0.12}Zn_{0.88}$	MgO
Zn-2.6Mg$^{(4h)}$	Powder	93.0	6.2	–	0.8
Zn-2.6Mg$^{(8h)}$	Powder	99.3	–	–	0.7
Zn-2.6Mg-0.6Ag$^{(4h)}$	Powder	92.8	6.4	<0.1	0.7
Zn-2.6Mg$^{(4h)+Ex}$	Compact	91.9	6.9	–	1.2
Zn-2.6Mg-0.6Ag$^{(4h)+Ex}$	Compact	92.2	7.0	<0.1	0.8

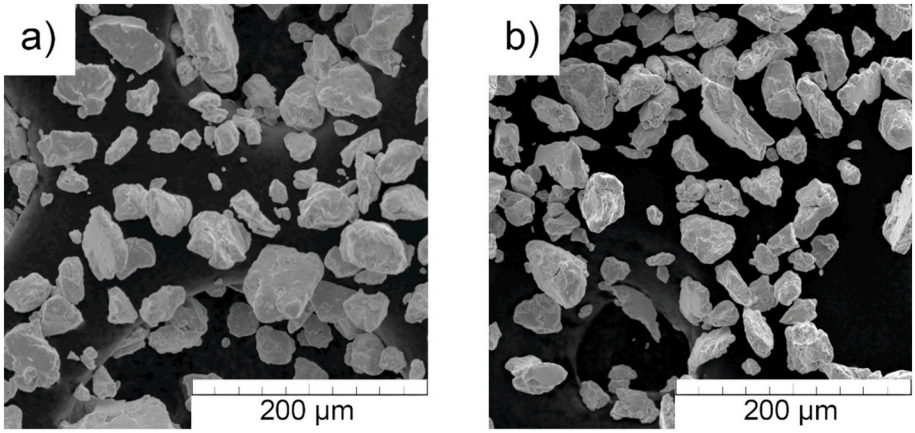

Fig. 1. Mechanically alloyed powders: A) Zn-2.6Mg$^{(4h)}$ B) Zn-2.6Mg-0.6Ag$^{(4h)}$.

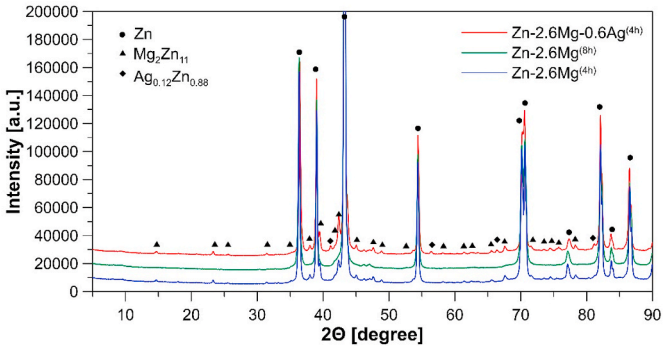

Fig. 2. XRD patterns of the Zn-2.6Mg-(0.6Ag) powders prepared by MA.

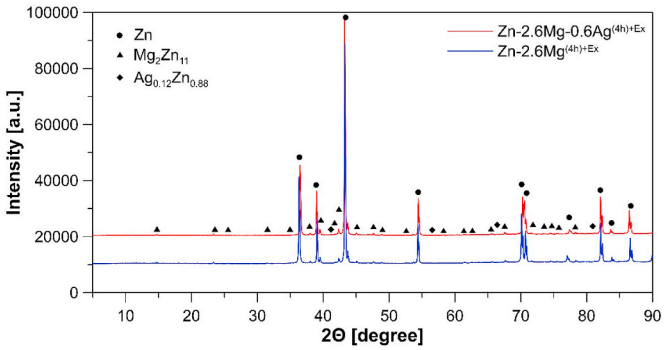

Fig. 3. XRD patterns of the Zn-2.6Mg-(0.6Ag) extruded materials.

peaks partially overlap with the Mg_2Zn_{11} phase at 36.9 and 42.9 °2θ positions, making them difficult to observe in XRD patterns. ZnO was not detected, although its presence under the detection limit cannot be excluded. It is worth mentioning that the alloy milled for 8 h suffered from extensive cracking during extrusion. This happened even with the processing temperature up to 400 °C. Therefore, Zn-2.6 $Mg^{(8h)+Ex}$ is not further studied in the paper.

3.1.2.1. Microstructure analyses using SEM with EDS and EBSD. As shown in the scanning electron micrographs in Fig. 4., both successfully synthesized (Zn-2.6$Mg^{(4h)+Ex}$ and Zn-2.6Mg-0.6$Ag^{(4h)+Ex}$) materials prepared by extrusion have an ultrafine-grained microstructure with a typical arrangement of intermediate phases in the rows parallel to the extrusion direction (Fig. 4a–d). Further figures of microstructure are shown in Fig. S3 – supplementary file. Firstly, the microstructure of both materials contained phases enriched by Mg with a size in the range of 0.3–1 μm (Fig. 4b and d). These phases were analyzed using SEM-EDS and contained about 14.6 at. % of Mg, which corresponds to the Mg_2Zn_{11} phase. Due to the size of these phases, their arrangement and confirmation of their presence in the powder precursor by XRD (Table 2), it is believed that they were formed during mechanical alloying. Indeed, the estimated content of Mg_2Zn_{11} in Zn–1$Mg^{(4h)}$ using Rietveld analyses of XRD was 15.1 at.%. Simple recalculation shows us that it corresponds to the 2.5 at.% of Mg in the alloy, indicating that Mg would be dissolved in the matrix in a very low concentration (≈0.1 at. %), further confirming that these phases are not formed during extrusion. Other smaller phases were observed in the microstructure mainly at the grain boundaries. Due to the existence of oxide shells on the surface of powder particles breaking during MA, these phases are expected to be oxide particles incorporated inside the microstructure during extrusion. This will be further discussed below.

The in-plane inverse pole figure (IPF) maps (Fig. 5) obtained by EBSD reveal the grain size and orientation. Both materials have comparable grain size distribution (Fig. 6) with the average grain size of 0.74 and 0.72 μm for Zn-2.6Mg and Zn-2.6Mg-0.6Ag, respectively. Both materials have very low texture strength with signs of $(01\bar{1}0)$ and $(\bar{1}2\bar{1}0)$ fiber texture (Fig. 7) and with the preferential orientation of basal planes parallel to the extrusion direction. However, the texture is much weaker compared to the Zn-based alloys prepared by conventional casting and wrought techniques (eg. hot extrusion, rolling, ECAP) [2,29,30]. Both, the presence of ultra-fine grains and more random distribution of crystallographic orientations are believed to be affected by the presence of intermediate phases in the size from tenths to hundreds of μm. To confirm this assumption further detailed analyses of the microstructure using APT and TEM were performed.

3.1.2.2. Detailed microstructure analyses using APT and TEM. The results of the APT analyses on the extruded materials are shown in Fig. 8 and Table 3. The Zn–1$Mg^{(4h)+Ex}$ sample contains mainly the Zn matrix and finely dispersed but unevenly distributed particles (Fig. 8a). The composition (at. %) of the different phases was obtained using profiles along a 5x5x4 nm cylinder with a bin size of 0.3 nm. Subsurface intermetallic particles show a Zn/Mg ratio consistent with the Mg_2Zn_{11} phase as reported in Table 3. Precipitate I (Fig. 8b), which intersects the specimen's surface is enriched in oxygen, mostly in the form of ZnO/Zn$(OH)_2$ ions in the APT analysis. Due to surface contamination during sample preparation and the presence of residual gas in the APT analysis chamber, accurate quantification of O and H is a known challenge and contributes to the variation of O and H on the surface layer [31–33]. Yet, this enrichment compared to the Zn phase, can be considered as indicative of preferential oxidation. The second intermetallic phase containing mostly Zn and Mg has Zn/Mg ratio inconsistent with equilibrium phases known in the Zn–Mg system and probably corresponds to the presence of an intermediate metastable phase. Fig. 8c is a composition profile using a 10x10x10 nm cylinder and a bin size of 0.3 nm showing a clear increase in Mg composition. These could be the formation of Guinier-Preston (GP) zones or clusters precursor to the intermetallic phase.

The results of APT analysis of the Zn-2.6Mg-0.6$Ag^{(4h)+Ex}$ shown in Fig. 8d indicate the presence of a Zn phase and an intermetallic phase with tenths of nm in size. The bulk composition (at%) of the phases was obtained by an analysis of a 5x5x4 nm cylinder and a 10x10x4 nm cylinder. The intermetallic phase corresponding to precipitate I-III (Fig. 8d) contains mostly Zn and Ag. Precipitate III has a composition consistent with the $Ag_{0.12}Zn_{0.88}$ ε-phase. No Ag-containing intermetallic phase was observed using XRD for the milled powder, whereas the presence of the ε-phase was confirmed by XRD in the extruded material indicating the precipitation of these phases during the extrusion. Fig. 8e and Fig. f, respectively suggest that grain boundaries and dislocations (Fig. S4 - supplementary file) are attractive segregation sites for Ag. The grain boundaries enriched with Ag are also decorated by clusters of Mg. The pattern formed by the assembly of Ag-segregated dislocations can be interpreted as a low-angle boundary as revealed by APT in other alloy systems [34–36].

TEM-EDS analyses of the Zn-2.6$Mg^{(4h)+Ex}$ revealed that nano-sized particles both at grain boundaries and inside the grains correspond to the Mg_2Zn_{11} and/or magnesium or zinc-enriched oxides (Fig. 9). These particles are smaller than the thickness of the lamellae, therefore the values of chemical composition estimated by EDS are affected by the surrounding matrix. For this reason, it is difficult to exactly distinguish oxide particles and the Mg_2Zn_{11} phase with oxidized surface as suggested by several APT observations. We believe that part of these particles come from the breakage of the oxide shells (ZnO) located at the surface of the powder precursors. This can be potentially the main source of observed ZnO inside the consolidated materials. XRD analyses of MA powder precursors (Table 2) also revealed the presence of MgO. This thermodynamically stable phase is preserved also in the consolidated materials. Mg_2Zn_{11} was also observed in the MA powder precursors, however, its content is slightly increased (Table 2) for

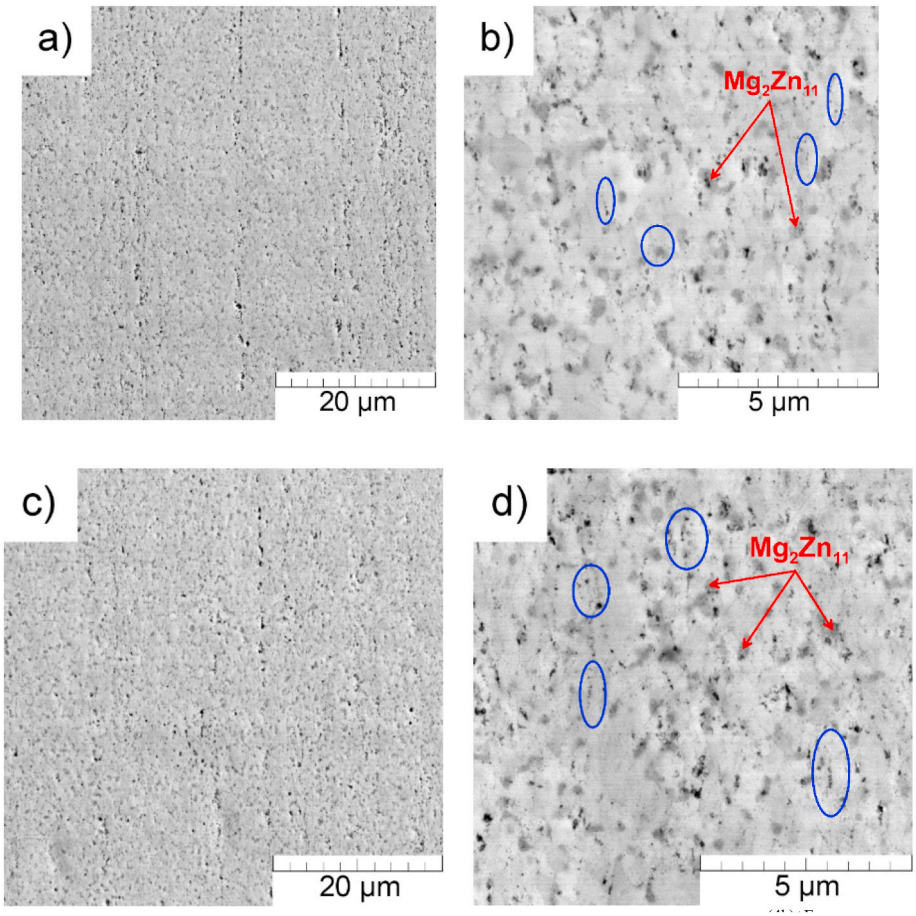

Fig. 4. Microstructure of the consolidated materials - SEM: a), b) Zn-2.6Mg$^{(4h)\ +\ Ex}$; c), d) Zn-2.6Mg-0.6Ag$^{(4h)\ +\ Ex}$; red arrows indicate Mg_2Zn_{11} phase, blue regions indicate the oxide particles pinning the grain boundaries.

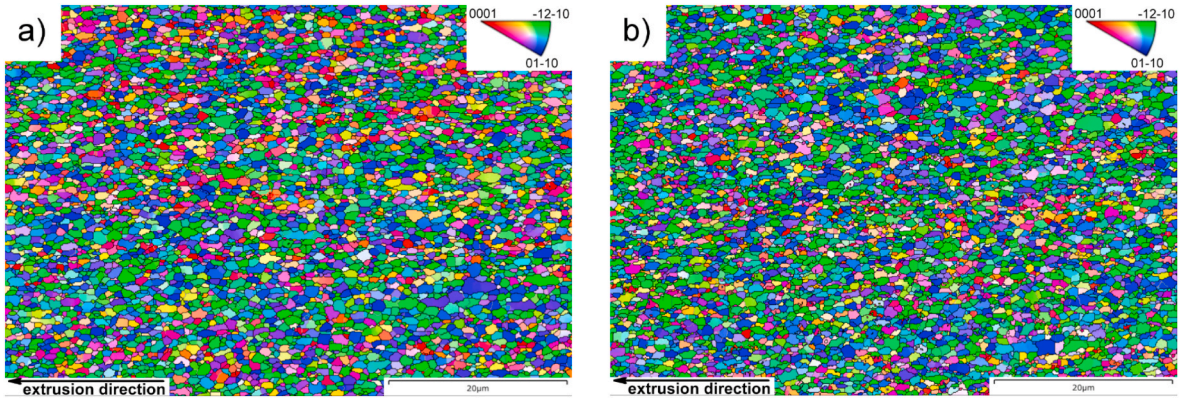

Fig. 5. IPF maps of the compacted materials: a) Zn-2.6Mg$^{(4h)\ +\ Ex}$, b) Zn-2.6Mg-0.6Ag$^{(4h)\ +\ Ex}$, extrusion direction is the reference direction of map.

consolidated materials. This may indicate the in-situ precipitation of this phase during the extrusion process. These results are supported by almost the extremely low amount of Mg dissolved in the zinc matrix measured by APT (Table 3). We were not able to distinguish between the oxides and intermetallic particles reliably, because of the image artefacts, low contrast difference and similar shape and size. In general, the secondary phases form particles of a size ranging between approximately 10 and 30 nm. The TEM analyses also revealed the Zn-based matrix contained large number of finer grains/subgrains with a size ranging between approximately 50 and 150 nm. The particles and precipitates help pin grain boundaries and, therefore, prevent microstructure coarsening. Although the temperature of the pre-consolidation and extrusion process was relatively high (200 °C), the presence of these particles is believed to be the main reason for the low average grain size (below 1 μm) in the extruded products.

3.2. Mechanical properties

The mechanical properties of the studied materials were evaluated based on tensile tests. The true stress-strain curves are plotted in Fig. 10a. Due to the similarities of measurements and for clarification, only one measurement from three is shown. Results considering average

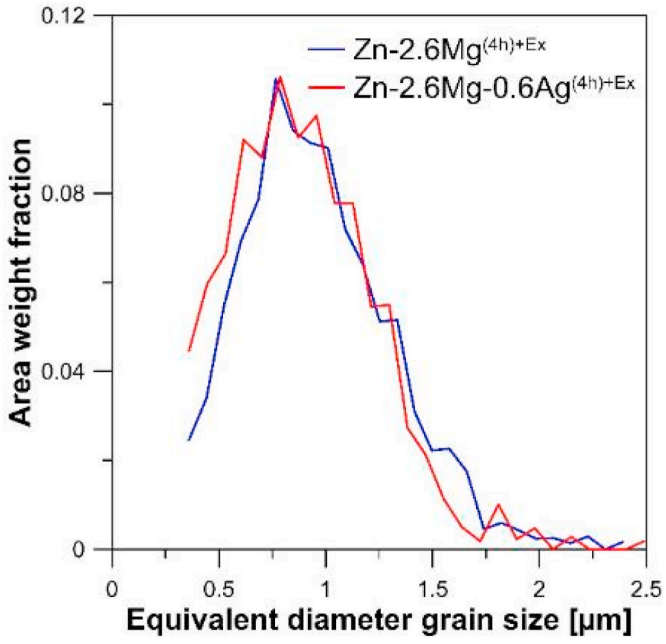

Fig. 6. The distribution of grain size: a) Zn-2.6Mg$^{(4h)\ +\ Ex}$, b) Zn-2.6Mg-0.6Ag$^{(4h)\ +\ Ex}$.

values and standard deviations are summarized in Fig. 10b and also supplementary data (Table S1 – supplementary file). Results for an extruded Zn-2.1Mg-1.15Sr alloy are added for comparison as an example of a widely studied alloy, with properties fulfilling requirements for integration in medical devices. This material was prepared by a common top-to-bottom approach (melting, homogenization annealing and hot extrusion), resulting in Zn mean grain size of approximately 2.5 μm [37,38]. Zn has a low melting temperature (420 °C), making 37 °C rather high homologous temperature for testing. To show the effect of temperature on mechanical properties, tensile tests at 37 °C have been performed for Zn-2.6Mg$^{(4h)\ +\ Ex}$ and also Zn-2.1Mg-0.15Sr^{Ex} as a reference alloy. Due to the limited quantity of material available following the preparation process, it was not possible to conduct tensile mechanical property measurements at 37 °C for the Zn-2.6Mg-0.6Ag$^{(4h)+Ex}$ alloy. The values of TYS (279 MPa) and UTS (384 MPa) for the Zn-2.6Mg$^{(4h)\ +\ Ex}$ exceed the performance of a majority of binary Zn–Mg or more complex alloys produced by conventional techniques like casting, extrusion, rolling [3]. Furthermore, the Zn-2.6Mg-0.6Ag$^{(4h)\ +\ Ex}$ alloy reached an 11 % higher value of TYS and 13 % higher value of UTS at almost similar elongation to fracture (E). Both Zn-2.6Mg$^{(4h)\ +\ Ex}$ and Zn-2.6Mg-0.6Ag$^{(4h)\ +\ Ex}$ showcase a significant increase in strength at the expense of their ductility. Minor deviations were observed among measurements for TYS, and UTS, although the ductility of Zn-2.6Mg-(0.6Ag)$^{(4h)\ +\ Ex}$ fluctuated more, suggesting that the microstructure of the prepared alloys was slightly heterogeneous and the secondary phases were locally concentrated, causing the increase in local internal stresses and decreased ductility.

It is evident from Table 2 and Fig. 10 that all Zn-based materials tested at 37 °C instead of laboratory temperature lose in mechanical performance significantly. The TYS and UTS values for Zn-2.1Mg-0.15Sr^{Ex} representing the reference material are decreased to 222 and 276 MPa which is even below the suggested tolerable values, while due to the generally higher mechanical strength of Zn–1Mg, the measured values of TYS and UTS at 37 °C correspond to the 246 MPa and 329 MPa, respectively. In summary, the decrease in mechanical strength is in both cases ≈14 %.

Comparing the shapes of the individual tensile curves (Fig. 10a), one can see that the curves of all powder metallurgical materials are of the same shape. Further data evaluation considering the true stress – true strain values are shown in Fig. S5 – supplementary file. Obtained results suggest that the deformation is accommodated by the same deformation mechanisms independent on the chemical composition and testing temperature. The reference alloy shows a significant increase in ductility after the increase in the testing temperature, while maintaining the general shape of the curve. To obtain more information, we treated the curves according to Ref. [39] and evaluated strain hardening coefficient n, strain hardening rate and dislocation storage density (Eqs. (1) and (2)).

$$\sigma = K \cdot \varepsilon^{n} \tag{1}$$

$$\theta = \frac{d\sigma}{d\varepsilon} \tag{2}$$

In these equations σ is normalized plastic true stress, ε is normalized plastic true strain, n is strain hardening coefficient, K is strength constant and θ hardening rate. The dislocation storage rate was evaluated as the slope of linear part of the hardening rate*normalized plastic stress vs. normalized plastic stress curves [39]. The plots showing various dependencies of mechanical behavior are shown in Fig. S4 (supplementary file) and the important values evaluated from those curves are listed in Table 4.

It is important to note that strengthening part of the curves belonging to powder metallurgical samples was very short and it was very difficult to distinguish the elasto-plastic and plastic deformation region, which could lead to the overestimation of the value of strain hardening coefficient.

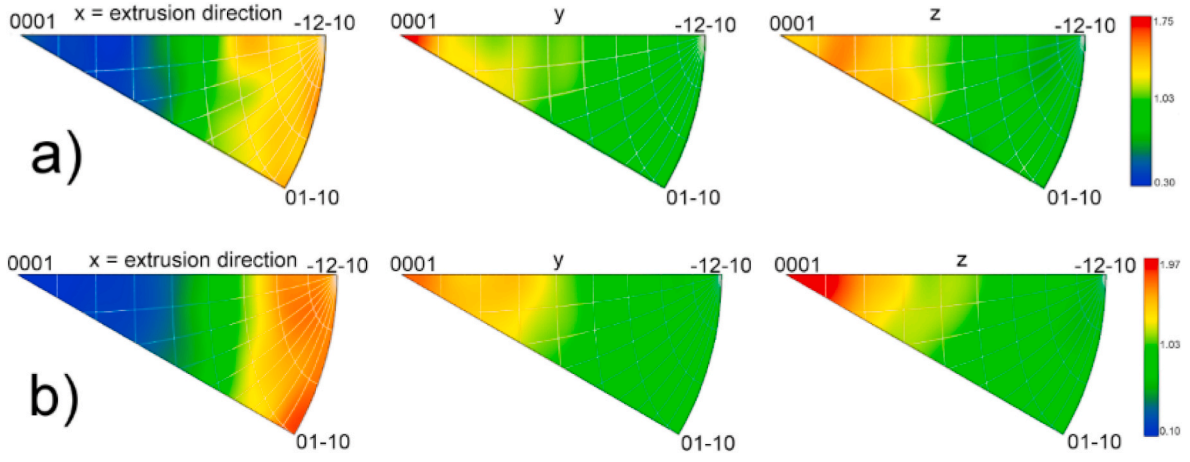

Fig. 7. The texture of studied materials presented by IPFs: a) Zn-2.6Mg$^{(4h)\ +\ Ex}$, b) Zn-2.6Mg-0.6Ag$^{(4h)\ +\ Ex}$.

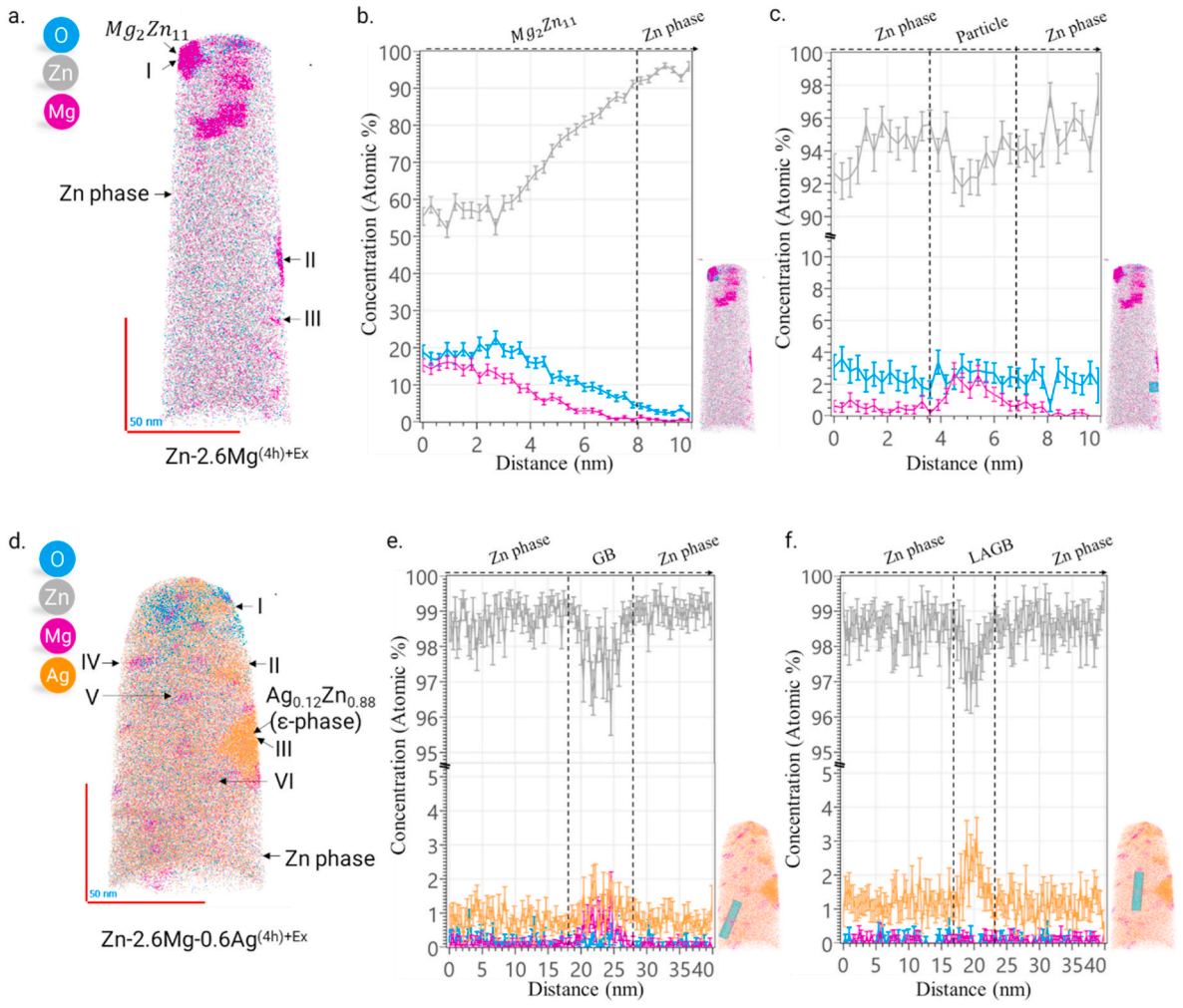

Fig. 8. Detailed analyses of extruded materials using APT: a) Zn-2.6Mg$^{(4h)\ +\ Ex}$; b) visualization of Mg_2Zn_{11} and Zn phase interface in Zn-2.6Mg$^{(4h)\ +\ Ex}$; c) visualization of nano-size particle and Zn phase interface in Zn-2.6Mg$^{(4h)\ +\ Ex}$ d) Zn-2.6Mg-0.6Ag$^{(4h)\ +\ Ex}$; e) visualization of grain boundary (GB) interface with Zn-2.6Mg-0.6Ag$^{(4h)\ +\ Ex}$ with a higher fraction of Mg ions; f) visualization of low-angle grain boundaries (LAGB) interface within Zn-2.6Mg-0.6Ag$^{(4h)\ +\ Ex}$ matrix with a higher fraction of Ag ions.

Table 3
Bulk compositional (at %) analysis obtained by APT measurements of Zn-2.6Mg$^{(4h)\ +\ Ex}$ and Zn-2.6Mg-0.6Ag$^{(4h)\ +\ Ex}$.

	Zn	Mg	Ag	O	H
Zn-2.6Mg $^{(4h)\ +\ Ex}$					
Bulk Zn	99.13	0.04		0.52	0.30
Precipitate I	57.80	12.48		19.00	10.72
Precipitate II	73.60	5.50		11.72	9.16
Precipitate III	94.81	2.10		1.74	1.35
Zn-2.6Mg-0.6Ag $^{(4h)\ +\ Ex}$					
Bulk Zn I	99.10		0.90		
Bulk Zn II	99.09		0.92		
Bulk Zn III	99.61	0.01	0.37	0.02	
Precipitate I	97.09	0.03	2.79	0.09	0.01
Precipitate II	98.14		1.93	0.03	
Precipitate III	88.81	0.05	11.13	0.01	
Precipitate IV	97.92	0.98	1.02	0.04	
Precipitate V	97.44	1.04	1.15	0.29	0.08
Precipitate VI	98.05	0.96	0.99		

3.3. Corrosion

The corrosion behavior of the Zn-2.6Mg$^{(4h)\ +\ Ex}$ and Zn-2.6Mg-0.6Ag$^{(4h)\ +\ Ex}$ was studied by performing a one-week exposure in an EMEM - medium simulating blood plasma, both in terms of similar inorganic ion content and biochemical component presence. After exposure, the materials were analyzed by SEM/EDS, then mechanical removal of bulk corrosion products was performed, and materials surface again analyzed by SEM/EDS (Fig. 11) and by OM (Fig. S6 – supplementary file).

From an overall perspective, there is a noticeable difference between the materials. The Zn-2.6Mg$^{(4h)\ +\ Ex}$ alloy shows significantly fewer changes compared to the original surface, the main ones being long fibrous deposits occupying a small part of the surface. Their shape indicates their protein origin. Zn-2.6Mg$^{(4h)\ +\ Ex}$ surface has observable furrows after grinding of the material. Their slightly blurred contours, together with the change in color of the material to blue-grey, indicate the presence of a thin film. According to the EDS, the thin film composition can be estimated to be predominantly a mixture of oxide and carbonate. Looking at the less abundant elements, apart from Mg with a lower abundance than in the bulk, the presence of calcium and phosphorus in approximately equiatomic proportions can be observed. Long fibrous deposits are also visible and their shape indicates their protein origin. After mechanical removal of the deposits, a localized attack site is observed with numerous small sharp-edged crevices and a larger central pit containing corrosion deposits. Here again, partially sharp edges referring to both initiation and propagation along the interfaces present in the material are observable, i.e. probably the Mg_2Zn_{11} phase surrounded by oxides. The composition of the corrosion products in the pit

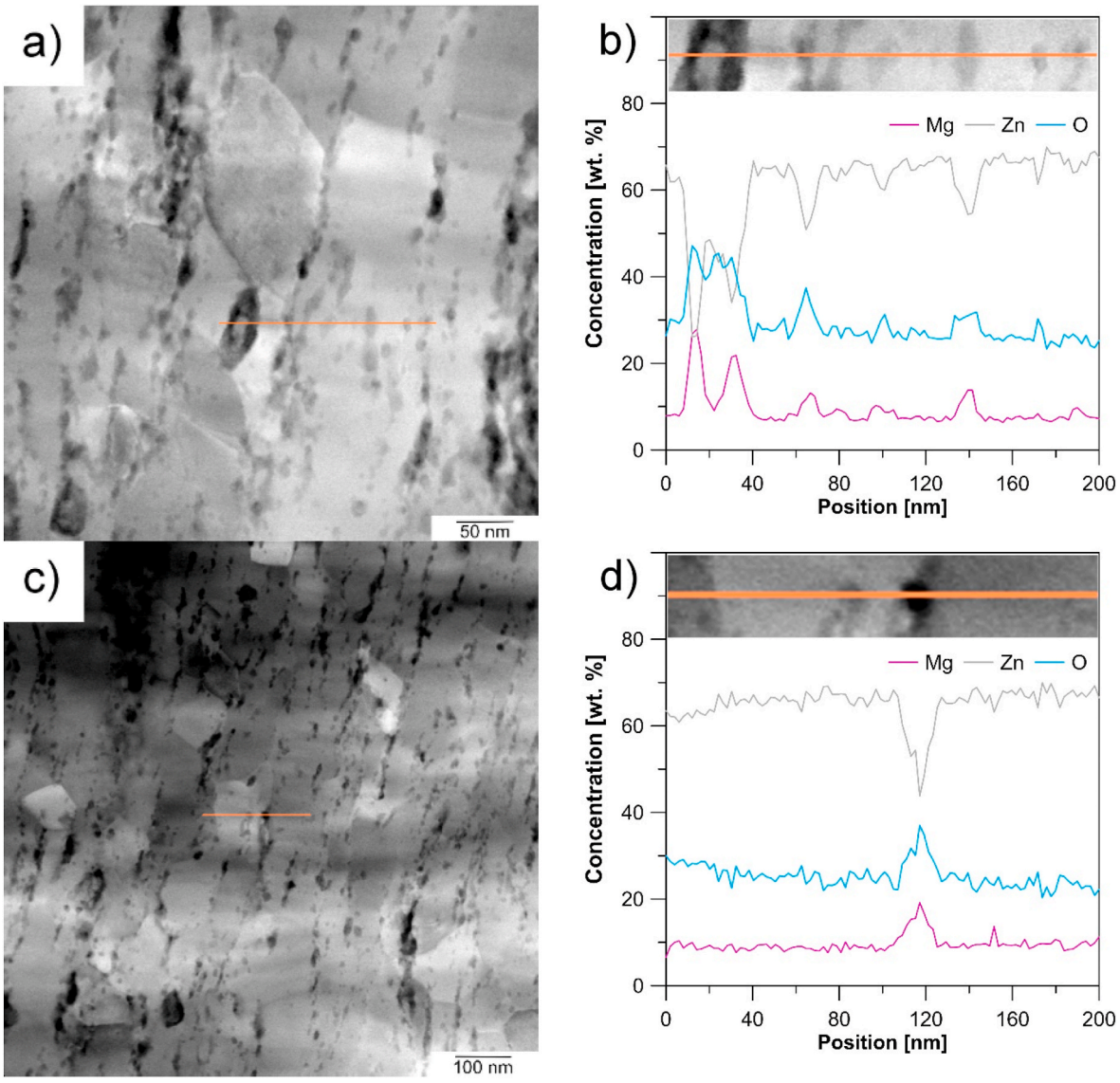

Fig. 9. Zn-2.6Mg$^{(4h)\ +\ Ex}$ microstructure analysis and profile of chemical composition along the orange line – STEM-EDS: a, b) location 1 and b, c) location 2.

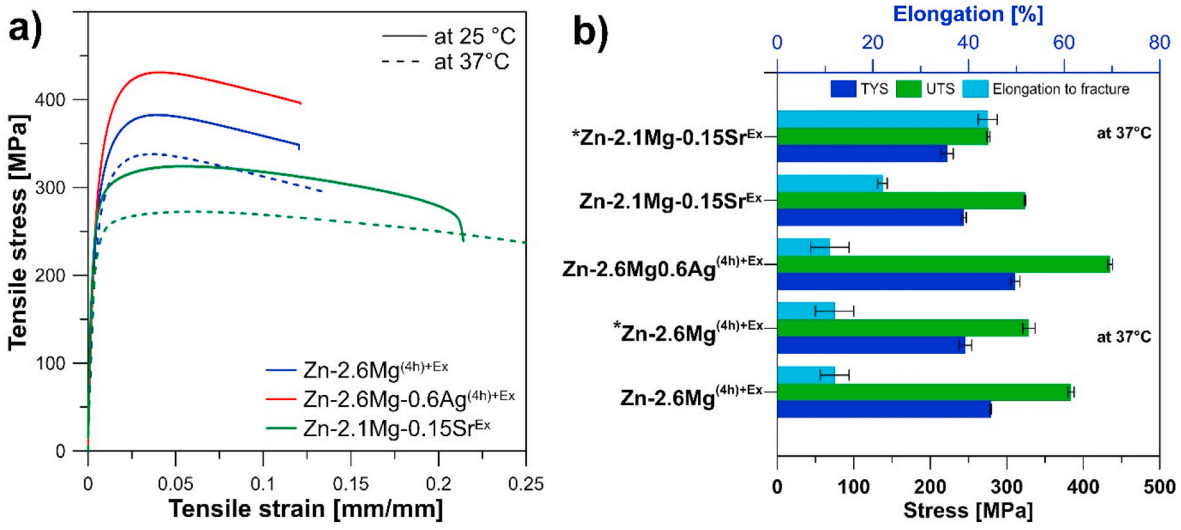

Fig. 10. Mechanical properties of materials: a) Tensile engineering stress – engineering strain curves at laboratory temperature and 37 °C (marked by *), b) evaluated properties of studied materials.

Table 4
Strengthening characteristics of the investigated materials.

	n	K (MPa)	strain at UTS (zero strengthening rate)	dislocation storage rate (m^{-2})
Zn-2.6Mg$^{(4h)+Ex}$	0.19	818	0.048	16139
[a]Zn-2.6Mg$^{(4h)+Ex}$	0.20	682	0.059	96030
Zn-2.6Mg-0.6Ag$^{(4h)+Ex}$	0.20	402	0.050	13173
Zn-2.1Mg-0.1Sr^{Ex}	0.05	402	0.090	91340
[a]Zn-2.1Mg-0.1Sr^{Ex}	0.06	344	0.138	97880

[a] tests performed at 37 °C.

indicates their predominantly chloride origin.

In the case of the Zn-2.6Mg-0.6Ag$^{(4h)+Ex}$ alloy, the frequency of attack sites is significantly higher, with a significant part surrounded by deposits. These deposits have only very occasionally a fibrous character. In addition, a macroscopic view of the less corroded regions reveals shallow rounded pits, outside of which a slight granulation can be observed on the surface. According to EDS, there is a higher abundance of non-silver elements, especially P and Ca, compared to the silver-free alloy. The concentration of Ag also increases to more than double in the round pits compared to the surrounding area. The majority of surface was again blue-grey in colour. After mechanical removal of the deposits, a larger and deeper pit is observed with sharp straight edges again filled with corrosion products. These, according to EDS, also contain significant amounts of P, Ag and Ca, in addition to abundant oxygen, supplemented by trace amounts of chlorine, sulphur and magnesium. It can therefore be assumed that the dominant compound is phosphate and, given the lower Ca/P ratio than 1, largely zinc.

The exposure was also supported by non-destructive electrochemical measurements whose results are summarized in Fig. 12a. The obtained spectra were evaluated using an equivalent circuit (Fig. 12b) based on a simple transmission-line model, with a physical interpretation based on the surface state observed in the SEM images after exposure (Fig. 11). In these circuits, the constant phase element (CPE) is used instead of a capacitor, which considers the non-ideal behavior of the system. The impedance of the constant phase element is defined as $1/Z = Y_0 (j\omega)^{\alpha}$, where $\alpha = (0; 1)$; if $\alpha = 1$, the CPE acts like a pure capacitor and if $\alpha = 0$, it acts as a pure resistor. The W (Warburg element) describing semi-infinite diffusion was also used for the evaluation.

The OCP for both materials after initial stabilization was around −0.96 V/SSCE, which corresponds to the standard reduction potential of zinc. This indicates high activity of zinc ions near the surface. However, there is a significant difference between the materials in terms of the corrosion current densities expressed in terms of R_P in Fig. 12a and the evaluation of impedance data accompanied by the evaluation of impedance data (Table S3 and Fig. S7 - supplementary file), where the main component of the total resistance is the charge transfer resistance (R_{ct}) following the R_P trend, there is a significant difference between the materials. The Zn-2.6Mg-0.6Ag$^{(4h)+Ex}$ material shows a two-to fourfold higher rate of reaction in this phase than Zn-2.6Mg$^{(4h)+Ex}$ material, with some fluctuations in the values of the silver-free alloy. In this case, the fluctuation may be due to two concurrent mechanisms. The first is the initiation of a local attack, followed by a slowing down of the rate by the formation of a barrier inside the pit. Under the present conditions, in agreement with the EDS analysis, the stable products are ZnO/$ZnOH_2$, $ZnCO_3$, and $ZnCl_2.4Zn(OH)_2$ or $ZnCl_2.6Zn(OH)_2$, whose precipitation is associated with a decrease in OCP, i.e. Zn^{2+} ion activity [40]. The second is the known transition in zinc oxide from the less protective type I to the more compact type II, and this change is reflected by a decrease in the barrier layer capacity to a two-thirds value. Additionally, the slight R_P fluctuation of Zn-2.6Mg$^{(4h)+Ex}$ between 36th and 96th hour of exposure can be attributed to the mechanism of folding of type I ZnO from the outer interface and is also noticeable in the oscillation of the size of the left, i.e., higher-frequency semicircle, involving the two outer time constants [41]. This phenomenon can again be linked mainly to the local attack sites since it is expressed most by changes in the right, low-frequency part of the spectrum – in terms of the EIS data evaluation by changes in the elements R_2 and W. From approximately 100 h of exposure onward, the system had already reached a stationary state, with the primary change being an increase in the capacitance of the external layer. Additionally, a decrease in its ideality was observed, as indicated by a reduction in the alpha parameter, which manifested as the theoretical higher-frequency semicircle compressing towards positive values of the imaginary part. The reason for this may be due to the precipitation of Ca–P-based compounds that are observable on the surface in the EDS analysis.

The higher charge exchange rates of Zn-2.6Mg-0.6Ag$^{(4h)+Ex}$ in the initial 36 h are accompanied by smaller sizes of all impedance semicircles. This is associated with three phenomena: a) higher frequency of primary attack sites; b) larger size of the pits formed; and c) formation of

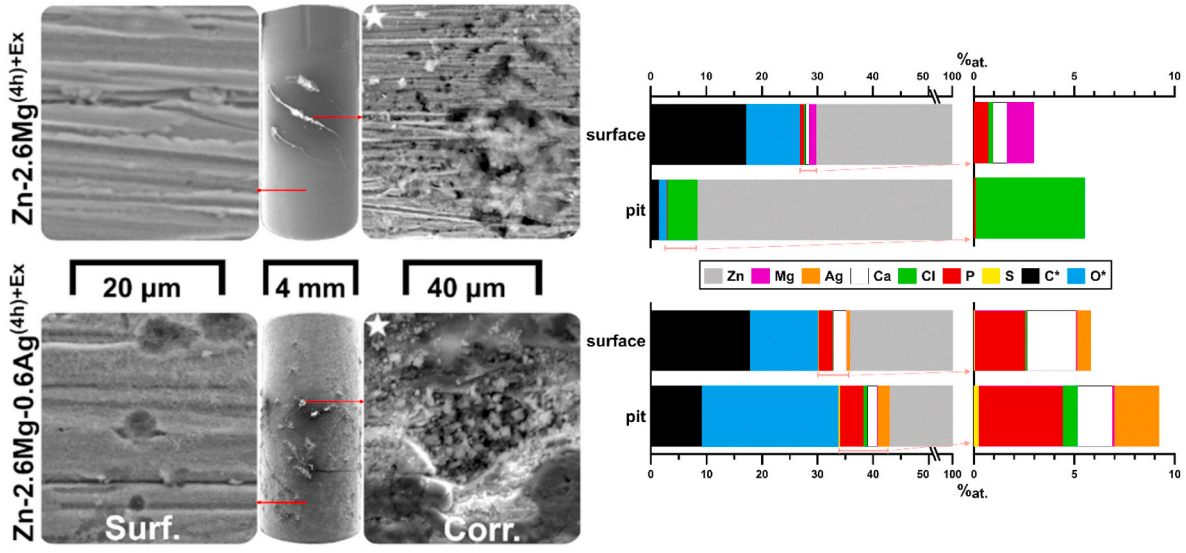

Fig. 11. a) SEM images after 7-day exposure in EMEM with 5 % FBS, ★ - after mechanical removal of fibrous deposits; b) EDS analysis of plain surface (Surf.) and corroded areas (Corr.) after 7-day exposure in EMEM with 5 % FBS: A - total; * - Analysis of light elements is only approximate.

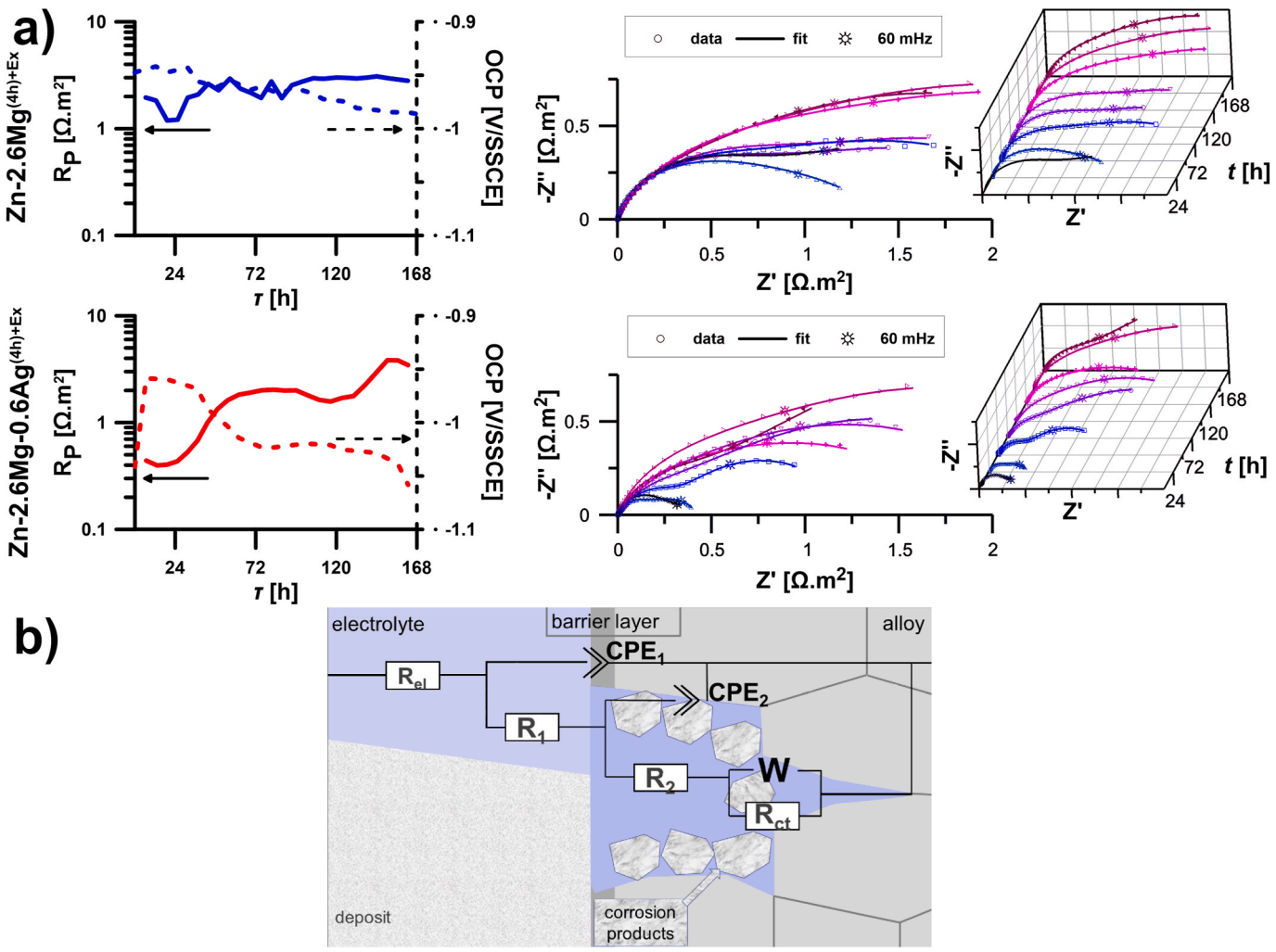

Fig. 12. Evolution of electrochemical behaviour of Zn-2.6Mg$^{(4h)+Ex}$; Zn-2.6Mg-0.6Ag$^{(4h)+Ex}$ during 7-day exposure in EMEM with 5 % FBS (top part); an equivalent circuit for evaluation of EIS data-bottom part.

precipitates around the pit entrance limiting transport between the bulk electrolyte and the pit. According to EDS analyses (Fig. 12b, Fig. S8 - supplementary file), this is due to the presence of the silver-containing phase, which, due to the galvanic effect, promotes the transition of the base metal to the ionic state. Between 24 and 36 h of exposure, there is a fivefold increase in R_P, associated with a growth of the right, low-frequency semicircle, caused mainly by an increase in R_{ct}. These changes are accompanied by a decrease in OCP, i.e. a decrease in Zn^{2+} ion activity. The probable cause, similarly to Zn-2.6Mg$^{(4h)+Ex}$, is the formation of stable corrosion products composed of oxygen and phosphorus, inside the sites of deep attack. These products were further transformed between 96 and 144 h, where both R_{ct} and R_P decreased due to concentration changes inside the pore. However, subsequently, around 136 h, this transformation is manifested by an increase in the barrier effect of the product within the pore. This is reflected in the spectra measured at 144 h by a significant increase in the low-frequency semicircle, which in terms of evaluation is related to the transformation of CPE_2 to an ideal capacitor with an order of magnitude lower capacitance values. This led in the subsequent measurement to a reduction of the effect of charge exchange and a dominant transition to diffusive control manifested by a typical straight line with a 45° slope. In terms of the outer layer, similarly to the silver-free alloy, there was an increase in capacitance from ca. 100 h, probably associated with the precipitation of the Ca–P-based layer.

The average surface corrosion rate (calculated using the final R_{ct} values and the mean Stern-Geary coefficient for active dissolution of 0.026) is 0.016 mm.a^{-1} and 0.011 mm.a^{-1} for the Zn-2.6Mg$^{(4h)+Ex)}$ and Zn-2.6Mg-0.6Ag$^{(4h)+Ex}$, respectively. Thus, there are no significant differences between the materials in this aspect.

3.4. *In vitro biological behavior*

3.4.1. *In vitro cytotoxicity test*

Test on extracts was performed using hFOB 1.19 cells in an L-15 medium. The undiluted extracts of the tested samples were not cytotoxic under the selected conditions (Fig. 13).

3.4.2. *Antibacterial tests*

Escherichia coli and *Staphylococcus epidermidis* were used to test the antibacterial effect of the investigated materials. The example results from the drip test (12 drops of bacterial suspension on each plate) are displayed in the supplementary file (Fig. S9 – supplementary file). Bacterial colonies were calculated in each drop and compared to the negative (unaffected) control. Fig. 14 shows the bacterial counts (CFU) of *E. coli* and *S. epidermidis* compared to the negative control. Cu used as a positive (antibacterial) control showed a significant antibacterial effect after 4 h of incubation. Zn-2.6Mg-0.6Ag$^{(4h)+Ex}$ showed a significant antibacterial effect against *S. epidermidis*. The set of samples was incubated in sole PBS for 4 h and there were no differences in the concentration of Zn released by AAS (Table S4).

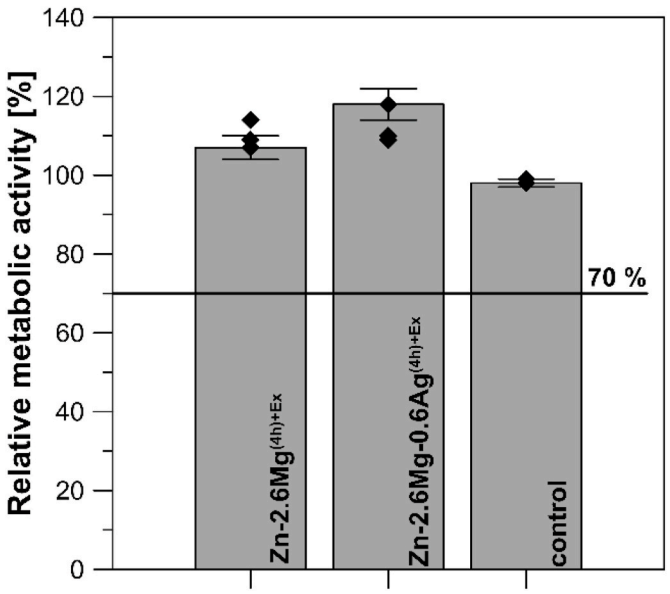

Fig. 13. Relative metabolic activity (resazurin test) of hFOB1.19 cells in medium L-15 after 1 day of incubation with undiluted extracts of the materials. The error bars express the sample standard deviation of 3 replicates used for each type of material. The normative limit represents 70 % of the metabolic activity of the unaffected control.

4. Discussion

4.1. Microstructure

Mechanical alloying is a well-known technique to form metastable alloys with a high volume of a solid solution for elements that exhibit limited solubility in the matrix [42]. The maximum equilibrium solubility of magnesium in zinc is approximately 0.27 at.% for a temperature of 364 °C [2] and it declines with decreasing temperature with the solubility of 0.02 at. % at 25 °C [7]. We found that after high-energy milling for 8 h at 800 RPM, all magnesium (2.6 at. %) was almost completely dissolved in the Zn matrix, and no Mg_2Zn_{11} or other Mg_xZn_y intermetallic phases were observed in the microstructure of the MA powder. However, the powder in presented conditions shows itself as inappropriate for subsequent processing by extrusion leading to strong cracking and tearing. This is probably related to the accumulation of Mg at grain boundaries and oxide particles leading to the loss of material ductility.

A shorter time of mechanical alloying at 800 RPM for 4h was here selected as suitable to prepare Zn-2.6Mg$^{(4h)}$ and Zn-2.6Mg-0.6Ag$^{(4h)}$ as a powder precursor for subsequent extrusion. Such powders contained thermodynamically stable Mg_2Zn_{11} phase with a size below 1 μm, therefore, significantly lower compared to the conditions in conventionally prepared materials.

In the as-cast state, the Mg_2Zn_{11} phase occurs in an eutectic mixture with Zn and forms a network at the η-Zn grain boundaries. After annealing, the eutectic phases are separated to decrease the Gibbs free energy of the system. As a result, particles with a size of several tens of micrometers distributed at grain boundaries are formed [3,43]. Although such coarse intermetallic phases can be further broken down by suitable thermomechanical or severe plastic deformation processing in the particles of a sub-micron size, they usually remain aligned into bands parallel with the direction of the shear stress applied during the treatment of the material, which can subsequently result in inhomogeneous deformation and environment-caused degradation [11,37,44]. This is important for mechanical properties while generally coarse Mg_2Zn_{11} can be a source of stress accumulation inside the material facilitating early fracture. The controlled temperature of the milling process (below 50 °C), the addition of stearic acid, and the incorporation of oxide particles in the microstructure during the process supported the creation of powders with a grain size of 480 and 520 nm for Zn-2.6Mg$^{(4h)}$ and Zn-2.6Mg-0.6Ag$^{(4h)}$, respectively (evaluated from XRD data by Rietveld analyses). This is in good agreement with our theoretical predictions based on a literature review, which are explained in the next paragraph in detail.

Burmeister et al. [45] investigated the characteristics of high energy ball milling using an Emax mill. Although they used slightly different powder/balls ratio, batch and different milling times, we can estimate, according to their results that the normal collision energy between two balls could be approximately 10^{-5} J, collision frequency about 10^3 s^{-1}. The total energy (E) introduced by ball collision is further estimated by a simple equation:

$$E = Energy\_collision * frequency\_collision * N\_balls * time \quad (3)$$

This results in the total deformation energy of approximately 7.2 kJ. Dividing by powder volume (4.2 ml), energy density, which is approximately equal to the deformation stress, is received [46]. Subsequently, the deformation stress (σ) can be substituted in the following equation for the estimation of minimum grain size obtainable by severe plastic deformation, where continuous dynamic recrystallization driven by dislocation slip is expected as the main recrystallization mechanism. The equation and all used constants are adopted from the work of Pinc et al. [11].

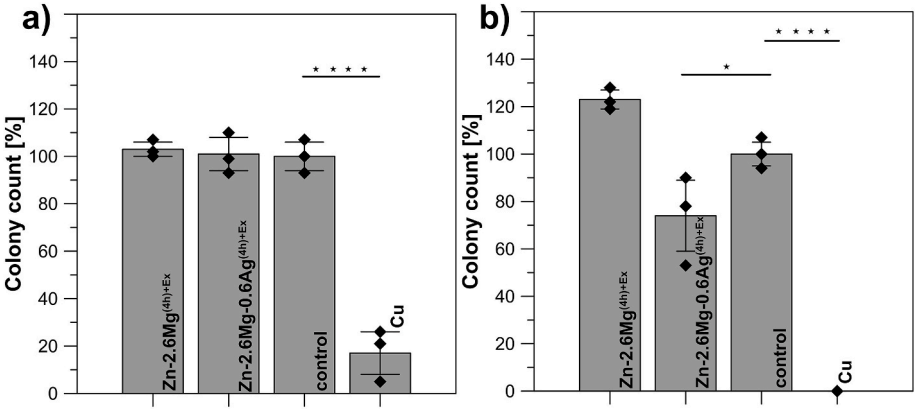

Fig. 14. Antibacterial activity expressed as colony numbers: a) *E. coli* and b) *S. epidermidis* (in %) compared to negative (unaffected) control after incubation with the materials. The error bars represent the standard deviation of three samples of each type. Differences from the negative control are indicated by an asterisk (one-way ANOVA followed by Dunnett's test),* stands for $p < 0.05$, ****stands for $p < 0.0001$.

$$\frac{d_{min}}{b} = A_3 e^{-\frac{\beta Q}{4RT}} \cdot \left(\frac{D_{PO} G b^2}{v_0 kT}\right)^{0.25} \cdot \left(\frac{\gamma}{Gb}\right)^{0.5} \cdot \left(\frac{G}{\sigma}\right)^{1.25} \quad (4)$$

For our estimations, we considered basal slip as the deformation mechanism and the material constants for pure zinc were used. The estimated minimum grain size obtained by this approach was approximately 300 nm. Considering the simplification included in the prediction approach, the obtained value is very close to the experimental ones.

The grain size evaluated by XRD includes the subgrains bounded by dislocation walls and low-angle boundaries. Therefore, the grain size obtained by EBSD can be larger. Although, due to the low recrystallization temperature of zinc and rather close value of grain size evaluated for compacted materials we consider this value as reliable. Even after compaction by extrusion, ultrafine-grained materials without porosity and with an average grain size of 720 and 740 nm for Zn-2.6Mg$^{(4h)}$ and Zn-2.6Mg-0.6Ag$^{(4h)}$, respectively, were achieved. The TEM observations have shown presence of many grains and subgrains with a size (evaluated in the normal direction to the extrusion axis) in the range 50–150 nm. The size of secondary phases ranged mainly between 10 and 30 nm and the sum of their volume fractions was approximately 5.7 vol% (calculated from XRD results and theoretical densities of the individual phases). Using the following equation (5),

$$d = \frac{c}{6^* f} \quad (5)$$

where c is dispersoid (secondary particles) diameter and f its volume fraction and considering the mean dispersoid diameter of 20 nm, the minimum grain size stabilized by the dispersoids is calculated [47]. This calculated as called Zenner grain size corresponds to 60 nm, which is in a good agreement with our observations and further supports our theory that the secondary particles are responsible for maintaining the fine microstructure after the processing at 200 °C.

Due to the low recrystallization temperature of zinc, it is challenging to achieve grain sizes smaller than a few μm by conventional up-to-bottom techniques. Although a rather high extrusion temperature of 200 °C was selected, no significant coarsening of the grains was observed due to the procedures' short duration and the pinning of the grain boundaries by the presented oxides and Mg_2Zn_{11} intermetallic phases. The particle (Smith-Zener) pinning is a common phenomenon in polycrystalline materials containing secondary phases and assuming some simplifications, it can be described as follows. In a closed system, the growth of certain grains must be accompanied by the shrinkage of other ones. If the grain boundary meets two precipitates, it stacks in those two points, while its rest is further moving to decrease the interface energy of the system and resulting in the straightening of the grain boundaries between the precipitates, reaching a stable state and suppressing further grain growth or shrinkage. As a result of a such process, equiaxed grains of a bimodal grain size distribution can be expected in the microstructure [48]. As is clearly visible in Fig. 4, both materials consisted of equiaxed grains with a bimodal size distribution and fine particles at the grain boundaries (Fig. 9) were observed by TEM and APT. This strongly supports our claim that particle pinning plays a very significant role in maintaining the ultra-fine microstructure after the hot extrusion.

Concerning other manufacturing techniques, only hydrostatic extrusion has been used to reach highly fine-grained material with a grain size of approximately 700 nm in the transverse direction and 1 μm in the extrusion direction [49]. The extrusion is also known to produce an anisotropic, directional, and highly textured microstructure in zinc alloys. In our case, no sharp texture components have been obtained for both extruded materials (Fig. 7). In crystallographic terms, a value of maximum intensity below 2 suggests that the grains have only a slight preference for certain orientations compared to a completely random distribution, where the maximum would be close to 1. We expect that the main reason is the presence of fine intermetallic phases and oxide particles, which enable particle-stimulated recrystallization and, at the same time, block the movement of the formed grain boundaries (Fig. 9).

To verify the recrystallized condition of the microstructure of extruded samples, the grain necessary dislocation map (GND) has been calculated using AZtecCrystal software and considering the slip in basal planes, which is the dominant slip system in hcp Zn (Fig. 15). These observations confirm that the grain interiors exhibit minimal strain, as evidenced by a low geometrically necessary dislocation (GND) density, approximately 10^{14} m^{-2}. In contrast, the grain boundaries demonstrate significant dislocation accumulation, represented by green regions, indicating that the grain interiors remain largely undeformed.

There exist technologies to form extremely fine-grained microstructures of Zn-based alloys, which rely on the effect of severe plastic deformation and dynamic recrystallization with the necessity of blocking particles to prevent grain coarsening. However, these materials were generally characterized by poor homogeneity, high porosity, excessive coarse oxide particles or strong texture. Zn-7.7Mg (at. %) alloys prepared by melt spinning technique using hot extrusion are characterized by non-homogeneous grain size distribution in the range from 100 nm to 4 μm and a network of oxides, which negatively affected mechanical behavior, especially the ductility of these materials [43]. Significant grain refinement can also be achieved by severe plastic deformation methods, including equal channel angular pressing (ECAP) [11,44], where the material is repeatedly pressed through a specific angle leading to intense plastic deformation. A Zn-4.2Mg (at. %) alloy produced by 4 ECAP passages at 150 °C resulted in zinc grain size and Mg_2Zn_{11} size of about 390 nm and 510 nm, respectively; however, the alloy possessed relatively poor elongation to fracture (5 %) related to the extremely strong material's texture [49]. The nano-grained (grain size 590 ± 60 nm) Zn–Mg alloys prepared by high-pressure torsion (HPT) are limited to a small volume of the resulting material and have high inhomogeneity of chemical and phase composition [50]. In the presented work, we have shown that an appropriate plastic deformation by the combination of MA and extrusion may lead to materials with dense and ultrafine-grained microstructure, where both Mg_2Zn_{11} and oxide particles help to increase microstructure stability and suppress the strong texture formation.

4.2. Mechanical properties

The mechanical properties of the prepared materials are affected by several main factors – the strengthening effect of grain boundaries, solid solution strengthening of zinc matrix by magnesium, the strengthening effect of intermediate phases (oxides, Mg_2Zn_{11}, ε-phase in Ag–Zn system), material texture, and residual stresses.

Both extruded materials were characterized by very similar average grain sizes close to 700 nm suggesting this contribution to be equivalent. The relationship between yield strength and grain size may be described based on the unified model considering grain boundary sliding [51]. In this equation, G represents the shear modulus, k is the Boltzmann's constant, b is the Burgers vector, δ is the grain boundary width, $\dot{\varepsilon}$ is deformation rate, D_{gb} represent grain boundary diffusion coefficient, T is thermodynamic temperature, and d_t is the grain size.

$$\sigma \approx \sqrt{\frac{\sqrt{3}GkT}{2d_t b^2} ln\left(\frac{\dot{\varepsilon} d_t^3}{2\delta D_{gb}} + 1\right)} \quad (1a)$$

To a first approximation, we can consider the behavior of materials according to the formula for pure Zn. This is reasonable due to the almost negligible content and low concentration of Mg and Ag, respectively, in solid solution. Subsequently, the calculated value for strengthening by grain boundaries would be approximately 186 MPa for both extruded alloys [51].

According to Chen et al. [52] Mg has a low strengthening effect in zinc. Therefore, the strengthening contribution by solid solution is considered to be 38 MPa representing an intrinsic value for pure zinc. In

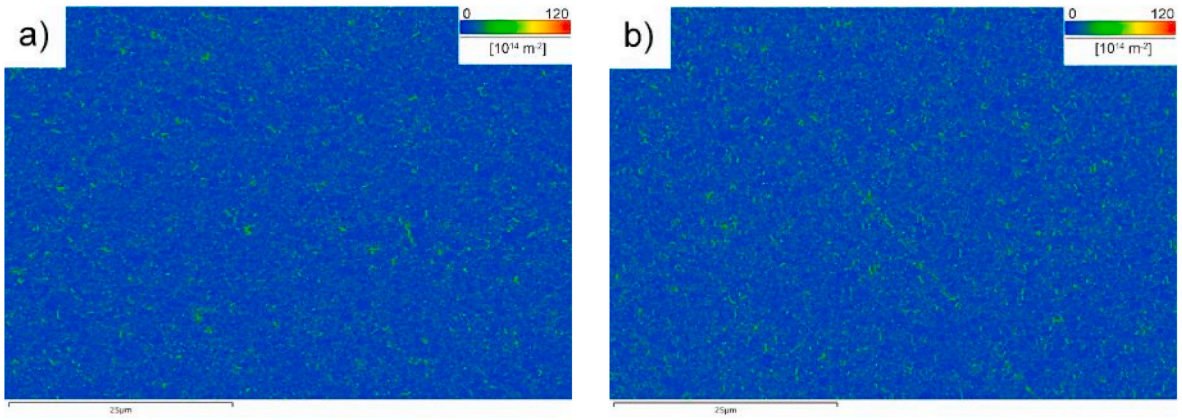

Fig. 15. Geometrically necessary dislocation (GND) map for: a) Zn-1.6Mg$^{(4h)\ +\ Ex}$; a) Zn-1.6Mg-0.6Ag$^{(4h)\ +\ Ex}$.

Zn–2.6Mg–0.6Ag alloy, Ag is further dissolved in zinc solid solution, however the strengthening effect with Ag content below 0.6 at % is rather small (≈15 MPa) [52].

The role of the residual stresses and texture is expected to be minor. As it was shown in Fig. 15, the materials are in recrystallized conditions, and therefore, no strong effects of internal stresses can be expected. Furthermore, a rather weak texture was observed. Therefore, residual strengthening contribution (55 MPa for Zn–1Mg and 72 for Zn–1Mg–1Ag) is assessed to the effect of phases (oxides, Mg_2Zn_{11}, ε-phase in Ag–Zn system). These phases can be divided into two groups. The first group is represented by phases predominantly distributed at grain boundaries and also bigger Mg_2Zn_{11} phases of similar size compared to the grains (<1 μm). In these cases, the strengthening effect can be overlapped with grain boundary strengthening. Although other intermetallic phases exist in the Zn–Mg system - MgZn, $MgZn_2$, Mg_7Zn_3, and Mg_2Zn_3 [53], none of these were observed in the microstructure or identified using XRD and APT. Mg_2Zn_{11} (space group - Pm-3, 330 HV0.01) [50] has a cubic structure, but the surrounding zinc matrix is hexagonal and the lattice parameters are highly different. For these reasons, we expect that the interface between Zn and Mg_2Zn_{11} will be semi-coherent or incoherent and the Orowan bypassing mechanism will contribute to the strengthening [54]. Another group is characterized by the presence of small Mg_xZn_y intermetallic precipitates (<35 nm) heterogeneously distributed within the Zn grains. These precipitates could not be crystallographically assigned to any known phases in the Zn–Mg system and may represent a metastable state during the formation of the thermodynamically stable Mg_2Zn_{11} phase. The presence of these metastable phases may induce localized stress variations across different grains under mechanical loading [55], potentially contributing to the observed variations in elongation to fracture under specific sample conditions.

The extrusion of Zn-2.6Mg resulted in the redistribution of oxides initially presented on the surface of the powder particles into the bulk material as finer oxide particles, with sizes in the range of hundreds of nanometers. XRD analysis confirmed the presence of MgO as a primary oxide phase, while advanced characterization techniques, such as TEM and APT, revealed the presence of Zn coexisting with Mg and O in specific microstructural features. This observation suggests the potential formation of mixed MgO/ZnO phases, as well as intermetallic phases with oxide layers on their surfaces.

The presence of MgO can be attributed to the high chemical affinity of magnesium for oxygen, driving Mg atoms from the solid solution towards oxygen atoms or molecules during the processing. This leads to the formation of MgO and potentially mixed Mg/Zn oxide phases. The mechanical contributions of these oxides remain challenging to quantify due to the complexity of their distribution and interactions. However, their preferential localization at grain boundaries is hypothesized to play a critical role in inhibiting excessive grain growth and stabilizing the ultrafine-grained microstructure.

In reaction to the state-of-the-art mechanical performance and microstructure analyses of Zn–Mg-based alloys, we bring the powerful material with one of the smallest stable grain sizes observed for zinc alloys and high elongation (≈12 %) together with high UTS (435 MPa). It is worth mentioning that this was even overcome by Jarzębska et al. [49] by processing as-cast Zn-2.6Mg by hydrostatic extrusion (Table 5.). Furthermore, Lin et al. [56] used novel way of Zn–Mg production while combining small Zn sheets with Mg powder in layers with subsequent accumulative rolled bonding (ARB). This procedure with 15 repetition of ARB led to the highest combination of TYS (540 MPa), UTS (560 MPa) and elongation to fracture (13 %) observed up to date for Zn-based alloys. These materials strongly differ in microstructure form studied materials by specific elongated grains and sharp texture in rolling direction, which may affect the mechanical properties. Mechanical properties of further Zn–Mg alloys with nominal content of Mg close to 2.6 at. % are shown in Table 5, while detailed information about other close materials with more complex chemical composition can be find in the review performed by Ji et al. [3].

The promising concept of our technology lies in the weaker material's texture and more uniform distribution of intermetallic phases and oxides in the microstructure. Because of those differences, more uniform and isotropic deformation and suppression of grain coarsening during

Table 5
Comparison of mechanical properties of Zn–Mg alloys prepared by different procedures.

Material (composition in at. %)	σTYS [MPa]	σUTS [MPa]	ε [%]	Source
Zn-2.6Mg$^{(4h)\ +\ E}$	280	386	12	This work
Zn-2.6Mg^{R}	190	240	12	[49]
Zn-2.6Mg^{E}	180	340	6	[49]
Zn-2.6Mg^{HE}	316	435	35	[49]
Zn-2.6Mg^{C}	-	147	1.5	[57]
Zn-2.6Mg^{C}	114	138	1	[58]
Zn-2.6Mg^{R}	217	226	12.5	[58]
Zn-2.6Mg^{E}	236	315	6.7	[59]
Zn-2.6Mg^{E}	180	215	18.5	[60]
Zn-2.6Mg^{E}	222	311	0.9	[29]
Zn-2.6Mg^{E}	289	320	32	[61]
Zn-2.6Mg^{HE}	383	482	23	[29]
Zn-2.6Mg$^{E\ +\ R}$	222	260	11.0	[62]
Zn-2.6Mg^{HE}	365	480	24.9	[63]
Zn-2.6Mg^{LPBF}	74	126	3.6	[64]
Zn-2.6Mg^{LPBF}	–	381	4.2	[65]
Zn-2.6Mg$^{CM,\ ARB}$	540	560	13	[56]

C – casting, E – extrusion, R – rolling, RS – rapid solidification, HE – hydrostatic extrusion, MA – mechanical alloying; LPBF – laser powder bed fusion; CM, ARB – composite materials, accumulative roll bonding.

the loading at elevated temperatures can be expected. In the case of fine-grain materials, the fine particles at the grain boundaries can also hinder deformation by grain boundary sliding. These together can help to suppress the anisotropy of mechanical properties and low-temperature creep.

Mechanical behavior of zinc and its alloys is very sensitive to temperature changes due to their low melting point. For pure Zn, the body temperature is about 0.45 of melting point and especially in the case of the materials with grain size in the submicron range, grain boundary sliding should be considered as a possible deformation mechanism [66]. Therefore, we performed the tensile tests at 37 °C, which is a temperature of human body environment. As a reference material, we used a Zn–Mg–Sr alloy prepared by a common, up to bottom way and possessing grain size of several micrometers. Such grain size was found to be fine sufficiently to suppress twinning, while maintaining resistant to the grain boundary sliding [37]. It is obvious in Fig. 10a, Fig. S5 – supplementary file and Table 3, that the strengthening behavior of all materials and at both temperatures followed the same trends. This suggests that the main deformation mechanisms are the same in all cases. The main difference was observed in the value of strain hardening coefficient of powder metallurgical and commonly prepared alloys. This coefficient ranged between 0.05 and 0.06 for the Zn–Mg–Sr alloy, while it reached values near to 0.2 for the materials produced by powder metallurgy. Strain hardening coefficient of several hundredths is commonly observed for Zn-based extruded alloys [67]. The high strain hardening coefficient of the powder metallurgical materials should be treated with a care, because it was very difficult to evaluate it due to the narrow interval of plastic strengthening. Although to describe the deformation mechanisms in the individual materials is beyond the scope of this article, the shapes of the obtained curves and their quantitative similarity suggest that in all cases dislocation slip is the main deformation mechanisms; however, a contribution of grain boundary sliding, recovery or recrystallization cannot be excluded.

4.3. Corrosion behavior

The addition of silver has a significant effect on the corrosion response of the material. When the rate of degradation in the initial part of the exposure is compared, the addition of silver leads to an order of magnitude increase, which results in more preferentially corroding sites and in a more uniform attack with increased silver content in these sites. In the case of Zn-2.6Mg-0.6Ag$^{(4h)\ +\ Ex}$, surface dissolution also occurred in areas that were otherwise likely to be completely blocked by a barrier layer composed of corrosion products and adsorbed biochemical components. However, due to the gradual blocking of preferential sites both externally by fibrous deposits and internally by the formation of insoluble barrier products, there was a slowing of the overall corrosion rate to 11 μm/year, which is low for millimeter-sized implants used in bone implantology but may be sufficient for biodegradable stents. Based on data from the literature, EDS and EIS results supported by thermodynamic simulations (Table S3, Figure S6 and Figure S10 - supplementary file), a very complex system of possible insoluble zinc corrosion products in a complex body medium is evident under static conditions, where oxides/hydroxides, hydrated chlorides/hydroxides, carbonates, phosphates can be formed [40]. This effect also applies in the case of the alloy containing 0.6 at% of Ag, where there is an increase in the frequency of attacked sites. This results in a uniform attack, associated with a shift in the equilibrium of corrosion products from basic chlorides to phosphates, which is associated with the precipitation of Ca–P based compounds known for their biocompatibility. This effect is likely attributed to a different initial interfacial response, where in the silver-containing alloy the formation of more substantial degradation products based on oxides/hydroxides is promoted, thereby limiting the potential blocking effect of the adsorbed organic component. When comparing the surface appearance of the alloys after corrosion testing, it is evident that the silver-free alloy exhibits only a slightly altered grinding pattern across most of the surface, whereas the silver-containing alloy shows a more pronounced modification of this pattern. This is related to the presence of corrosion products, both over the general surface and frequently in the form of macroscopic deposits. Such observation is consistent with degradation experiments on zinc and its silver-containing alloys in the presence of organic components – typically under in vivo conditions – where a significantly greater amount of corrosion products is observed for silver-containing zinc alloys. According to EDS mapping, these products predominantly consist of zinc and oxygen [53,54].

4.4. In vitro biological behaviour

Materials synthesized via powder metallurgy were evaluated for cytotoxicity and antibacterial efficacy. In a previous study, extracts of these materials were tested in various media using two cell lines, L929 and hFOB 1.19, using a surface-to-volume ratio of 0.875 cm^2 mL^{-1}. The undiluted extracts demonstrated significant toxicity, nearly eliminating the metabolic activity of both cell lines. However, a two-fold dilution of the extracts restored metabolic activity in hFOB 1.19 cells to levels exceeding the normative threshold [68].

In this study, the L-15 medium was employed as an alternative environment for investigating the corrosion behaviour and biological response of biodegradable zinc-based alloys. The extracts prepared in L-15 medium, using a reduced surface-to-volume ratio of 0.25 cm^2 mL^{-1}, showed no cytotoxic effects. This observation is attributed to the lower concentration of Zn^{2+} ions in the medium, as well as the high amino acid content of L-15, which binds Zn^{2+} and mitigates direct cellular interactions.

The antibacterial activity of the materials was assessed using *Escherichia coli* (Gram-negative) and *Staphylococcus epidermidis* (Gram-positive) as representative microorganisms. Notably, the Zn-2.6Mg-0.6Ag$^{(4h)\ +\ Ex}$ sample exhibited a significant reduction in the colony count of *S. epidermidis*. This effect may be due to the higher sensitivity of *S. epidermidis* to Ag, as observed in our prior studies [68,69]. Further investigations into the behaviour of zinc alloys in L-15 medium compared to other environments are ongoing and will be reported separately.

5. Conclusions

Zinc-magnesium-(silver) materials were successfully prepared by powder metallurgy methods, including MA and extrusion. Combining these methods significantly affects materials' properties, leading to the following conclusions.

1) Mechanical alloying of Zn–Mg and Zn–Mg–Ag for 4 h led to the formation of ultrafine-grained microstructure with Mg_2Zn_{11} phase and oxide particles containing both Mg and Zn.
2) Prolonged mechanical alloying (8 h) leads to the enhanced dissolution of Mg in zinc solid solution.
3) Ultrafine-grained microstructure preserved for Zn–1Mg$^{(4h)\ +\ Ex}$ and Zn–1Mg–1Ag$^{(4h)\ +\ Ex}$ consolidated materials with a grain size of ≈700 nm. Mg_2Zn_{11} phases were observed as particles with size below 150 nm and larger ones below 1 μm.
4) Extruded materials contained fully recrystallized microstructure and weak crystallographic texture located on the right side of the inverse pole figure triangle.
5) The extruded materials demonstrated a balanced combination of mechanical properties, with Zn–1Mg and Zn–1Mg–1Ag alloys achieving yield strengths of 279 MPa and 311 MPa, ultimate tensile strengths of 376 MPa and 435 MPa, and elongations to fracture of 12 % in both cases.
6) The TYS and UTS of Zn–1Mg dropped about 12 and 15 % at 37 °C, respectively. Obtained values of 246 MPa and 329 MPa still make the material interesting for further corrosion and biological studies related to applications like bioabsorbable medical devices.

7) Silver presence in alloy supports the antibacterial effect towards *S. epidermidis*.

Author contributions

Jiří Kubásek – data analyses, mechanical tests, writing, review, editing, Selase Torkornoo – APT analyses, writing, review, editing, David Nečas – materials preparation using SPS, microstructure analyses using OM, Ingrid McCarroll – APT analyses, Vojtěch Hybášek – corrosion tests, Baptiste Gault – APT data analysis, review, editing, Eva Jablonská – in-vitro biological tests, writing, Črtomir Donik – EBSD analyses, Irena Paulin – microstructure analyses using SEM, Peter Gogola – XRD analyses, Martin Kusý – XRD analyses, Zdeněk Míchal – in-vitro biological tests, Jaroslav Fojt – corrosion tests, Miroslav Čavojský – materials preparation by extrusion, Jan Duchoň – TEM analyses and their evaluation, Markéta Jarošová – EDX, WDX analyses, Jaroslav Čapek – processing and interpretation of TEM data, review, editing.

Declaration of competing interest

The authors declare the following financial interests/personal relationships which may be considered as potential competing interests: Jiri Kubasek, David Necas, Vojtech Hybasek, Eva Jablonska, Jaroslav Fojt, Jaroslav Capek reports financial support was provided by Czech Science Foundation. Crtomir Donik, Irena Paulin reports financial support was provided by Slovenian Research and Innovation Agency. Miroslav Cavojsky reports financial support was provided by Ministry of Education Science Research and Sport of the Slovak Republic. Jiri Kubasek, Eva Jablonska, Jaroslav Fojt reports financial support was provided by Ministry of Education Youth and Sports of the Czech Republic. If there are other authors, they declare that they have no known competing financial interests or personal relationships that could have appeared to influence the work reported in this paper.

Acknowledgement

This research was supported by the Czech Science Foundation (project no. 21–11439K) and by the project "Mechanical Engineering of Biological and Bio-inspired Systems", funded as project No. CZ.02.01.01/00/22_008/0004634 by Programme Johannes Amos Comenius, call Excellent Research. Furthermore, this work was carried out within the framework of the Slovenian Research Agency ARIS project N2-0182 ‘‘Development of advanced bioabsorbable Zn-based materials by powder metallurgy techniques. ‘‘and ARIS program P2 0132 ‘‘Physics and Chemistry of Metals‘‘. Baptiste Gault, Ingrid McCarroll and Selase Torkornoo are grateful to the Deutsche Forschungsgemeinschaft (DFG) for funding through Baptiste Gault’s Leibniz Award. The Slovak authors would like to thank the Vega 1/0531/22 project funded by the Ministry of Education, Science, Research and Sport of the Slovak Republic for the financial support and Cost action CA22147 (EU4MOFs).

Appendix A. Supplementary data

Supplementary data to this article can be found online at https://doi.org/10.1016/j.jmrt.2025.06.185.

References

[1] Kabir H, Munir K, Wen C, Li Y. Recent research and progress of biodegradable zinc alloys and composites for biomedical applications: biomechanical and biocorrosion perspectives. Bioact Mater 2021;6(3):836–79.
[2] Mostaed E, Sikora-Jasinska M, Drelich JW, Vedani M. Zinc-based alloys for degradable vascular stent applications. Acta Biomater 2018;71:1–23.
[3] Ji C, Ma A, Jiang J, Song D, Liu H, Guo S. Research status and future prospects of biodegradable Zn-Mg alloys. J Alloy Compd 2024;993.
[4] Chen Q, Thouas GA. Metallic implant biomaterials. Mater Sci Eng R Rep 2015;87:1–57.
[5] Li H, Zheng Y, Qin L. Progress of biodegradable metals. Prog Nat Sci Mater Int 2014;24(5):414–22.
[6] Li HF, Xie XH, Zheng YF, Cong Y, Zhou FY, Qiu KJ, Wang X, Chen SH, Huang L, Tian L, Qin L. Development of biodegradable Zn-1X binary alloys with nutrient alloying elements Mg, Ca and Sr. Sci Rep 2015;5:1–14.
[7] Jin H, Zhao S, Guillory R, Bowen PK, Yin Z, Griebel A, Schaffer J, Earley EJ, Goldman J, Drelich JW. Novel high-strength, low-alloys Zn-Mg (\textless 0.1wt \% Mg) and their arterial biodegradation. Materials science \& engineering C, Materials for biological applications 2018;84:67–79.
[8] Agarwal R, Fries SG, Lukas HL, Petzow G, Sommer E, Chart TG, Effenberg G. Assessment of the Mg-Zn system. International Journal of Materials Research 1992;83(4):216–23.
[9] Suryanarayana C, Ivanov E, Boldyrev VV. The science and technology of mechanical alloying. Materials Science and Engineering: A 2001;304–306:151–8.
[10] da Rocha CJ, Neto RML, Gonçalves VS, Carvalho LL, Ambrozio Filho F. An investigation of the use of stearic acid as a process control agent in high energy ball milling of Nb-Al and Ni-Al powder mixtures. Materials Science Forum 2003;416–418:144–9.
[11] Pinc J, Školáková A, Veřtát P, Duchoň J, Kubásek J, Lejček P, Vojtěch D, Čapek J. Microstructure evolution and mechanical performance of ternary Zn-0.8Mg-0.2Sr (wt. %) alloy processed by equal-channel angular pressing. Materials Science and Engineering: A 2021;824.
[12] Narendra Kumar Y, Venkateswarlu B, Ratna Raju L, Dumpala R, Ratna Sunil B. Developing Zn-MgO composites for degradable implant applications by powder metallurgy route. Materials Letters 2021;302.
[13] Bahraminasab M, Farahmand F. State of the art review on design and manufacture of hybrid biomedical materials: hip and knee prostheses. Proceedings of the Institution of Mechanical Engineers, Part H: Journal of Engineering in Medicine 2017;231(9):785–813.
[14] Lee K-H, Lee J-M, Park J-H, Kim B-M. Fabrication of miniature helical gears by powder extrusion using gas atomized Zn–22%Al powder. Transactions of Nonferrous Metals Society of China 2012;22(6):1313–21.
[15] Qiu CL, Attallah MM, Wu XH, Andrews P. Influence of hot isostatic pressing temperature on microstructure and tensile properties of a nickel-based superalloy powder. Materials Science and Engineering: A 2013;564:176–85.
[16] Sotoudeh Bagha P, Khaleghpanah S, Sheibani S, Khakbiz M, Zakeri A. Characterization of nanostructured biodegradable Zn-Mn alloy synthesized by mechanical alloying. J Alloy Compd 2018;735:1319–27.
[17] Yan Y, Liu H, Fang H, Yu K, Zhang T, Xu X, Zhang Y, Dai Y. Effects of the intermetallic phases on microstructure and properties of biodegradable magnesium matrix and zinc matrix prepared by powder metallurgy. Materials Transactions 2018;59(11):1837–44.
[18] Li XY, Zhang ZH, Cheng XW, Huo GJ, Zhang SZ, Song Q. The development and application of spark plasma sintering technique in advanced metal structure materials: a review. Powder Metallurgy and Metal Ceramics 2021;60(7–8):410–38.
[19] Cheng Y, Cui Z, Cheng L, Gong D, Wang W. Effect of particle size on densification of pure magnesium during spark plasma sintering. Advanced Powder Technology 2017;28(4):1129–35.
[20] Cui Z, Luo M, Zhang Y, Gong D, Wang W, Wang J. Fabrication of high strength and plasticity of Zn-Mg composites with core–shell structure by spark plasma sintering. Materials Letters 2020;279.
[21] Yang Y, Yuan F, Gao C, Feng P, Xue L, He S, Shuai C. A combined strategy to enhance the properties of Zn by laser rapid solidification and laser alloying. J Mech Behav Biomed Mater 2018;82:51–60.
[22] Voshage M, Megahed S, Schückler PG, Wen P, Qin Y, Jauer L, Poprawe R, Schleifenbaum JH. Additive manufacturing of biodegradable Zn-xMg alloys: effect of Mg content on manufacturability, microstructure and mechanical properties. Materials Today Communications 2022;32.
[23] Qin Y, Liu A, Guo H, Shen Y, Wen P, Lin H, Xia D, Voshage M, Tian Y, Zheng Y. Additive manufacturing of Zn-Mg alloy porous scaffolds with enhanced osseointegration: in vitro and in vivo studies. Acta Biomater 2022;145:403–15.
[24] Vojtech D, Kubasek J, Serak J, Novak P. Mechanical and corrosion properties of newly developed biodegradable Zn-based alloys for bone fixation. Acta Biomaterialia 2011;7(9):3515–22.
[25] Lutterotti L, Matthies S, Wenk HR. MAUD (Naturiel Analysis Using Diffraction): a user friendly JAVA program for Rietveld texture analysis and more. 1999. p. 1599–604.
[26] Fischer J, Pröfrock D, Hort N, Willumeit R, Feyerabend F. Improved cytotoxicity testing of magnesium materials. Materials Science and Engineering: B 2011;176(11):830–4.
[27] Školáková A, Pinc J, Jablonská E, Školáková T, Veřtát P, Janebová B, Kutová A, Čapek J, Hosová K, Vojtěch D, Kubásek J. A zinc phosphate layered biodegradable Zn-0.8Mg-0.2Sr alloy: characterization and mechanism of hopeite formation. Surface and Coatings Technology 2024;487.
[28] Necas D, Marek I, Pinc J, Vojtech D, Kubasek J. Advanced zinc-magnesium alloys prepared by mechanical alloying and spark plasma sintering. Materials (Basel) 2022;15(15).
[29] Jarzębska A, Bieda M, Maj Ł, Chulist R, Wojtas D, Strąg M, Sułkowski B, Przybysz S, Pachla W, Sztwiertnia K. Controlled grain refinement of biodegradable Zn-Mg alloy: the effect of magnesium alloying and multi-pass hydrostatic extrusion preceded by hot extrusion. Metallurgical and Materials Transactions A 2020;51(12):6784–96.
[30] Kubasek J, Vojtech D, Jablonska E, Pospisilova I, Lipov J, Ruml T. Structure, mechanical characteristics and in vitro degradation, cytotoxicity, genotoxicity and mutagenicity of novel biodegradable Zn-Mg alloys. Mater Sci Eng C-Mater Biol Appl 2016;58:24–35.

[31] Kim S-H, Bhatt S, Schreiber DK, Neugebauer J, Freysoldt C, Gault B, Katnagallu S. Understanding atom probe's analytical performance for iron oxides using correlation histograms and ab initio calculations. New Journal of Physics 2024;26(3):033021.
[32] Gault B, Saksena A, Sauvage X, Bagot P, Aota LS, Arlt J, Belkacemi LT, Boll T, Chen Y-S, Daly L, Djukic MB, Douglas JO, Duarte MJ, Felfer PJ, Forbes RG, Fu J, Gardner HM, Gemma R, Gerstl SSA, Gong Y, Hachet G, Jakob S, Jenkins BM, Jones ME, Khanchandani H, Kontis P, Krämer M, Kühbach M, Marceau RKW, Mayweg D, Moore KL, Nallathambi V, Ott BC, Poplawsky JD, Prosa T, Pundt A, Saha M, Schwarz TM, Shang Y, Shen X, Vrellou M, Yu Y, Zhao Y, Zhao H, Zou B. Towards establishing best practice in the analysis of hydrogen and deuterium by atom probe tomography. Microscopy and Microanalysis December 2024;30(6):1205–20.
[33] Devaraj A, Colby R, Hess WP, Perea DE, Thevuthasan S. Role of photoexcitation and field ionization in the measurement of accurate oxide stoichiometry by laser-assisted atom probe tomography. The Journal of Physical Chemistry Letters 2013;4(6):993–8.
[34] Araullo-Peters VJ, Gault B, Shrestha SL, Yao L, Moody MP, Ringer SP, Cairney JM. Atom probe crystallography: atomic-scale 3-D orientation mapping. Scripta Materialia 2012;66(11):907–10.
[35] Yu Y, Zhang S, Mio AM, Gault B, Sheskin A, Scheu C, Raabe D, Zu F, Wuttig M, Amouyal Y, Cojocaru-Mirédin O. Ag-segregation to dislocations in PbTe-based thermoelectric materials. ACS Applied Materials & Interfaces 2018;10(4):3609–15.
[36] Kwiatkowski da Silva A, Leyson G, Kuzmina M, Ponge D, Herbig M, Sandlöbes S, Gault B, Neugebauer J, Raabe D. Confined chemical and structural states at dislocations in Fe-9wt%Mn steels: a correlative TEM-atom probe study combined with multiscale modelling. Acta Materialia 2017;124:305–15.
[37] Kubásek J, Pinc J, Hosová K, Straková M, Molnárová O, Duchoň J, Nečas D, Čavojský M, Knapek M, Godec M, Paulin I, Vojtěch D, Čapek J. The evolution of microstructure and mechanical properties of Zn-0.8Mg-0.2Sr alloy prepared by casting and extrusion. J Alloy Compd 2022;906.
[38] Klima K, Ulmann D, Bartos M, Spanko M, Duskova J, Vrbova R, Pinc J, Kubasek J, Vlk M, Ulmannova T, Foltan R, Brizman E, Drahos M, Beno M, Machon V, Capek J. A complex evaluation of the in-vivo biocompatibility and degradation of an extruded ZnMgSr absorbable alloy implanted into rabbit bones for 360 days. International Journal of Molecular Sciences 2021;22(24).
[39] Zhao C, Chen X, Pan F, Wang J, Gao S, Tu T, Liu C, Yao J, Atrens A. Strain hardening of as-extruded Mg-xZn (x = 1, 2, 3 and 4 wt%) alloys. Journal of Materials Science & Technology 2019;35(1):142–50.
[40] Zhang XG. Electrochemical thermodynamics and kinetics. In: Zhang XG, editor. Corrosion and electrochemistry of zinc. Boston, MA: Springer US; 1996. p. 19–63.
[41] Zhang XG. Passivation and surface film formation. In: Zhang XG, editor. Corrosion and electrochemistry of zinc. Boston, MA: Springer US; 1996. p. 65–91.
[42] Vaidya M, Muralikrishna GM, Murty BS. High-entropy alloys by mechanical alloying: a review. Journal of Materials Research 2019;34(5):664–86.
[43] Capek J, Kubasek J, Pinc J, Drahokoupil J, Cavojsky M, Vojtech D. Extrusion of the biodegradable ZnMg0.8Ca0.2 alloy - the influence of extrusion parameters on microstructure and mechanical characteristics. J Mech Behav Biomed Mater 2020;108:16.
[44] Pinc J, Skoláková A, Hybásek V, Msallamová S, Vertát P, Ashcheulov P, Vondrácek M, Duchon J, McCarroll I, Hyvl M, Banerjee S, Drahokoupil J, Kubásek J, Vojtech D, Capek J. A detailed mechanism of degradation behaviour of biodegradable as-ECAPed Zn-0.8Mg-0.2Sr with emphasis on localized corrosion attack. Bioactive Materials 2023;27:447–60.
[45] Burmeister CF, Hofer M, Molaiyan P, Michalowski P, Kwade A. Characterization of stressing conditions in a high energy ball mill by discrete element simulations. Processes 2022;10(4).
[46] Martelli S, Di Nunzio PE. Powder ball milling: an energy balance approach to particle size reduction. Journal of Materials Research 2024;40(2):292–308.
[47] Schneibel JH, Heilmaier M. Hall-petch breakdown at elevated temperatures. Materials Transactions 2014;55(1):44–51.
[48] Bignon M, Bernacki M. Particle pinning during grain growth—a new analytical model for predicting the mean limiting grain size but also grain size heterogeneity in a 2D polycrystalline context. Acta Materialia 2024;277.
[49] Jarzębska A, Bieda M, Kawałko J, Rogal Ł, Koprowski P, Sztwiertnia K, Pachla W, Kulczyk M. A new approach to plastic deformation of biodegradable zinc alloy with magnesium and its effect on microstructure and mechanical properties. Materials Letters 2018;211:58–61.
[50] Hernández-Escobar D, Rahman ZU, Yilmazer H, Kawasaki M, Boehlert CJ. Microstructural evolution and intermetallic formation in Zn-Mg hybrids processed by High-Pressure Torsion. Philosophical Magazine 2018;99(5):557–84.
[51] Figueiredo RB, Kawasaki M, Langdon TG. Seventy years of Hall-Petch, ninety years of superplasticity and a generalized approach to the effect of grain size on flow stress. Progress in Materials Science 2023;137.
[52] Chen C, Fan S, Niu J, Huang H, Jin Z, Kong L, Zhu D, Yuan G. Alloying design strategy for biodegradable zinc alloys based on first-principles study of solid solution strengthening. Materials & Design 2021;204.
[53] Kammerer CC, Behdad S, Zhou L, Betancor F, Gonzalez M, Boesl B, Sohn YH. Diffusion kinetics, mechanical properties, and crystallographic characterization of intermetallic compounds in the Mg–Zn binary system. Intermetallics 2015;67:145–55.
[54] Liu H, Huang H, Zhang Y, Xu Y, Wang C, Sun J, Jiang J, Ma A, Xue F, Bai J. Evolution of Mg–Zn second phases during ECAP at different processing temperatures and its impact on mechanical properties of Zn-1.6Mg (wt.%) alloys. J Alloy Compd 2019;811.
[55] Deschamps A, Hutchinson CR. Precipitation kinetics in metallic alloys: experiments and modeling. Acta Materialia 2021;220.
[56] Lin J, Chen Y, Dai Y, Zhang X, Zhang D, Li Y, Wen C. Mechanical properties, degradation action, and biocompatibility of in situ nanoparticle-reinforced Mg(x)Zn(y)/Zn composite prepared via roll bonding. Acta Biomater 2025;194:514–29.
[57] Kubasek J, Vojtěch D. Zn-based alloys as an alternative biodegradable materials. Proc Metal 2012;5:23–5.
[58] Tong X, Zhang D, Lin J, Dai Y, Luan Y, Sun Q, Shi Z, Wang K, Gao Y, Lin J, Li Y, Dargusch M, Wen C. Development of biodegradable Zn–1Mg–0.1RE (RE = Er, Dy, and Ho) alloys for biomedical applications. Acta Biomater 2020;117:384–99.
[59] Pan C, Sun X, Xu G, Su Y, Liu D. The effects of β-TCP on mechanical properties, corrosion behavior and biocompatibility of β-TCP/Zn-Mg composites. Materials Science and Engineering: C 2020;108:110397.
[60] Zhao R, Ma Q, Zhang L, Zhang J, Xu C, Wu Y, Zhang J. Revealing the influence of Zr micro-alloying and hot extrusion on a novel high ductility Zn–1Mg alloy. Materials Science and Engineering: A 2021;801:140395.
[61] Li R, Ding Y, Zhang H, Lei J, Shen Y. Effective strengthening and toughening in Zn–1Mg alloy with bimodal grain structure achieved by conventional extrusion. Materials Science and Engineering: A 2022;854:143850.
[62] García-Mintegui C, Córdoba LC, Buxadera-Palomero J, Marquina A, Jiménez-Piqué E, Ginebra M-P, Cortina JL, Pegueroles M. Zn-Mg and Zn-Cu alloys for stenting applications: from nanoscale mechanical characterization to in vitro degradation and biocompatibility. Bioactive Materials 2021;6(12):4430–46.
[63] Pachla W, Przybysz S, Jarzębska A, Bieda M, Sztwiertnia K, Kulczyk M, Skiba J. Structural and mechanical aspects of hypoeutectic Zn–Mg binary alloys for biodegradable vascular stent applications. Bioactive Materials 2021;6(1):26–44.
[64] Cui J, Liang H, Chen S, Shao Y, Chen H, Yang M, Yang Y. Recent progress and perspectives in laser additive manufacturing of biodegradable zinc alloy. Journal of Materials Research and Technology 2024/11/01;33.
[65] Voshage M, Megahed S, Schückler PG, Wen P, Qin Y, Jauer L, Poprawe R, Schleifenbaum JH. Additive manufacturing of biodegradable Zn-xMg alloys: effect of Mg content on manufacturability, microstructure and mechanical properties. Materials Today Communications 2022;32:103805.
[66] Balog M, Marques de Castro M, Čapek J, Švec Jr P, Takáčová M, Csáderová L, Sedláčková E, Švastová E, Školáková A, Dvorský D, Pinc J, Hybásek V, Kubásek J, Krížik P, Skiba J, Bajana O, Hassan Ibrahim AM. Suppression of mechanical instability in bioabsorbable ultrafine-grained Zn through in-situ stabilization by ZnO nanodispersoids. Journal of Materials Research and Technology 2023;25:4510–27.
[67] Bednarczyk W, Wtroba M, Kawako J, Baa P. Can zinc alloys be strengthened by grain refinement? A critical evaluation of the processing of low-alloyed binary zinc alloys using ECAP. Materials Science and Engineering A 2019;748(December 2018):357–66.
[68] Jablonska E, Mrazkova L, Kubasek J, Vojtech D, Paulin I, Ruml T, Lipov J. Characterization of hFOB 1.19 cell line for studying Zn-based degradable metallic biomaterials. Materials (Basel) 2024;17(4).
[69] Švagrová K, Horkavcová D, Jablonská E, Helebrant A. Titania-based sol-gel coatings with Ag, Ca-P applied on titanium substrate developed for implantation. J Biomed Mater Res B Appl Biomater 2022;110(1):115–24.